

Quarterly Technical Report

Solid State Research

2000:4

Lincoln Laboratory

MASSACHUSETTS INSTITUTE OF TECHNOLOGY

LEXINGTON, MASSACHUSETTS



Prepared for the Department of the Air Force under Contract F19628-00-C-0002.

Approved for public release; distribution is unlimited.

20010612 092


This report is based on studies performed at Lincoln Laboratory, a center for research operated by Massachusetts Institute of Technology. The work was sponsored by the Department of the Air Force under Contract F19628-00-C-0002.

This report may be reproduced to satisfy needs of U.S. Government agencies.

The ESC Public Affairs Office has reviewed this report, and it is releasable to the National Technical Information Service, where it will be available to the general public, including foreign nationals.

This technical report has been reviewed and is approved for publication.

FOR THE COMMANDER


Gary Tutungian
Administrative Contracting Officer
Plans and Programs Directorate
Contracted Support Management

Non-Lincoln Recipients

PLEASE DO NOT RETURN

Permission is given to destroy this document
when it is no longer needed.

Massachusetts Institute of Technology
Lincoln Laboratory

Solid State Research

Quarterly Technical Report

1 August — 31 October 2000

Issued 15 May 2001

Approved for public release; distribution is unlimited.

Lexington

Massachusetts

AQM01-09-1576

ABSTRACT

This report covers in detail the research work of the Solid State Division at Lincoln Laboratory for the period 1 August through 31 October 2000. The topics covered are Quantum Electronics, Electro-optical Materials and Devices, Submicrometer Technology, Biosensor and Molecular Technologies, Advanced Imaging Technology, Analog Device Technology, and Advanced Silicon Technology. Funding is provided by several DoD organizations—including the Air Force, Army, BMDO, DARPA, Navy, NSA, and OSD—and also by the DOE, NASA, and NIST.

TABLE OF CONTENTS

Abstract	iii
List of Illustrations	vii
List of Tables	x
Introduction	xi
Reports on Solid State Research	xiii
Organization	xxiii
1. QUANTUM ELECTRONICS	1
1.1 Passive Temperature Compensation in Critically Phase-Matched Harmonic Generation	1
2. ELECTRO-OPTICAL MATERIALS AND DEVICES	5
2.1 Measurement of Mode-Locked Laser Timing Jitter Using Phase-Encoded Optical Sampling	5
2.2 Two-Dimensional Model of Surface-Energy-Induced Mass Transport	11
3. SUBMICROMETER TECHNOLOGY	19
3.1 Microscopy at Wavelengths Below 200 nm	19
3.2 Studies of Laser-Induced Contamination and Cleaning	23
4. BIOSENSOR AND MOLECULAR TECHNOLOGIES	29
4.1 Response of B Cells to Superparamagnetic Particle Simulants	29
5. ADVANCED IMAGING TECHNOLOGY	35
5.1 A 32×32 Laser Radar Imager Based on a Geiger-Mode Avalanche Photodiode Array Integrated with a CMOS Digital Timing Circuit	35

6.	ANALOG DEVICE TECHNOLOGY	41
6.1	Intermodulation Distortion in YBCO Bicrystal Grain Boundaries	41
7.	ADVANCED SILICON TECHNOLOGY	45
7.1	Back-End-of-the-Line Scaling for Silicon-on-Insulator CMOS	45

LIST OF ILLUSTRATIONS

Figure No.		Page
1-1	Diagram of passive temperature compensation concept.	2
1-2	Difference between $\theta(T)$ and $d(T)$ for three incidence angles on the prism.	2
1-3	Experimental conversion efficiencies for compensated and uncompensated harmonic generation.	3
2-1	Phase-encoded optical sampling system consisting of harmonically mode-locked fiber laser, 1:4 optical time-division demultiplexers, detect and integrate circuits, 12-bit quantizers (AD6640), buffer memory, and computer control. The additional amplitude modulator is included to investigate laser-amplitude-noise suppression.	7
2-2	Power spectra of optically sampled data with artificially induced laser amplitude noise: intensity sampling (top) and phase-encoded sampling (bottom). Amplitude-noise suppression due to phase-encoded sampling is 60 dB. The 3-GHz amplitude modulation “noise” signal aliases to 13.86 MHz for the sampling rate of 52 MS/s.	8
2-3	Power spectra of optically sampled data for the following inputs: 3-GHz sinusoid (top) and no signal (bottom). Note the noise floor increase (dotted line) and the pattern noise spurs (indicated by arrows) when the sinusoid is present.	9
2-4	Power spectra of individual pattern noise spur for intensity sampling (top) and phase-encoded sampling (bottom). Dotted lines show the calculated frequency of the pattern-noise spur.	10
2-5	Illustration of surface profile and cylindrical coordinates used in this work, where the transformation of the profile due to surface-energy-induced mass transport is considered.	12
2-6	Universal profile that characterizes the time evolution of an initial δ -function.	17
2-7	Evolution of single cylindrical mesa of radius a and height A_0 as predicted in the present model.	17
3-1	Spectrum of rf microdischarge lamp operating in an ArF atmosphere. Inset: schematic of the device showing small ($\sim 100\ \mu\text{m}$) region of excited gas between two electrodes.	19

LIST OF ILLUSTRATIONS (Continued)

Figure No.		Page
3-2	Images of thin films taken at 193 nm and in white light: (a) 5-nm layer of poly(hydroxystyrene) (pHOST) on a Si substrate taken at 193 nm; the pHOST is the darker region. (b) Image of the same field as in (a) taken in white light; the pHOST is undetectable. Note the Cr alignment feature at the bottom right of each image. (c) 1-nm layer of pHOST on a transparent quartz substrate. The difficulty of obtaining uniform illumination is apparent in this image. (d) 3-nm layer of thermally grown SiO_x on Si. The theoretical contrast of this image is only ~4% (see Figure 3-3).	21
3-3	Calculated reflection contrast, where R_1 and R_2 are the low and high reflectivity, respectively, for (a) pHOST on Si, (b) Si_3N_4 on Si, (c) SiO_x on Si, and (d) pHOST on quartz. Note the clear advantage of deep-ultraviolet illumination over near ultraviolet and visible in each case.	22
3-4	Schematic drawing of the contamination exposure system. Contaminants are introduced into the purge stream flowing through the vapor cell using calibrated permeation membrane devices. Four separate flow controllers are used to independently control dilution, oxygen level, and contaminant residence times within the vapor cell. With this arrangement, contamination levels can be conveniently controlled between 100 ppb and 10 ppm and oxygen levels between 0 and 50 ppm. A Fourier transform infrared (FTIR) based gas phase analysis system monitors the exhaust from the vapor cell to confirm contamination levels. Pressures within the vapor cell are held slightly above atmosphere to prevent any potential contaminants within the optical test bed from leaking into the vapor cell.	24
3-5	Transmission data collected with the contamination exposure system. In this experiment, 400 ppb of toluene was introduced into the purge gas flowing in the vapor cell. For clarity, this and subsequent graphs show the resulting transmission change over one CaF_2 window of the vapor cell.	25
3-6	Transmission change as the oxygen level is varied between 0.4 and 13 ppm in 3 ppm of toluene. After the first 1000 J/cm^2 , the contaminant arm of the gas delivery manifold is turned off and full transmission was restored.	26
3-7	Estimated contamination rate based on the transmission data taken in Figure 3-6 after first monolayer is deposited.	26
4-1	Typical perfusion chamber experimental setup: (a) Schematic of chamber setup. (b) Photomicrograph of B cells (large spheres) and $2.8\text{-}\mu\text{m}$ -diam phosphoryl choline (PC)/SA-beads (small spheres) mixed at a ratio of 4 beads/cell.	30

LIST OF ILLUSTRATIONS (Continued)

Figure No.		Page
4-2	Dose-response behavior of stimulation of adhered B cells with PC/SA-beads. The numbers used to label each curve represent the average number of beads/cell in each individual experiment plotted.	31
4-3	Increased photon output after release of approximately 1000 localized PC/SA-beads.	32
4-4	Increased photon output after active magnetic capture of ≤ 3000 beads delivered in 150- μ l volume.	33
5-1	Photomicrograph of portion of 32×32 array of CMOS timing circuits.	36
5-2	Block diagram of timing circuit, which consists of 15-bit pseudorandom counter, and clock phase detection circuitry to measure subperiod time intervals.	36
5-3	Photomicrograph of 32×32 bridge-bonded avalanche photodiode (APD)/CMOS laser radar imager.	37
5-4	“Negative-tone” images obtained by illumination of the imager with patterns of steady light.	38
5-5	Image obtained by illumination of portion of imager with timed pulse of green light from light-emitting diode (top), and corresponding timing histogram (bottom).	39
6-1	Plot of $1/Q_u$ as a function of rf current at $T = 50$ K. The curves are largely indistinguishable until the rf current reaches a level where the grain boundary (GB) causes the $1/Q_u$ to increase compared to the film on the single-crystal substrate. This increase is only seen in the 24° and 10° grain boundary.	41
6-2	Schematic view of resonator used in the experiments. The engineered grain boundary is located at the midpoint of the patterned line.	42
6-3	Results of measurement of third-order intermodulation distortion (IMD) power at 30 K for the various grain-boundary angles as shown. We plot IMD power vs output power at the fundamental, P_{out} . The 24° grain boundary shows a marked increase in IMD, but the other angles do not show any systematic variation. From this we conclude that the low-angle grain boundaries are not the source of IMD in epitaxial thin films.	43
7-1	Resist reflectivity (a) without antireflection coating (ARC) and (b) with ARC.	47
7-2	Exposure latitude vs depth of focus for different resists and mask biases.	48

LIST OF ILLUSTRATIONS (Continued)

Figure No.		Page
7-3	Normalized depth vs etch time for contact holes of sizes 500 nm ($y = -0.0065x^2 + 6.503x$), 350 nm ($y = -0.0074x^2 + 6.1097x$), and 275 nm ($y = -0.0094x^2 + 5.8427x$).	49
7-4	Normalized etch rate vs aspect ratio for contact holes of sizes 500, 300, and 200 nm.	50
7-5	Scanning electron micrograph (SEM) cross section of 0.27- μm contact etched in 0.8 μm of oxide.	51
7-6	Cross-sectional SEM of 0.27- μm tungsten-filled contact plug.	53
7-7	SEMs of 0.17/0.225- μm etched metal stack.	53

LIST OF TABLES

Table No.		Page
3-1	Calculated Deposition Rates at 3 ppm of Toluene	27
7-1	Design Rules	46

INTRODUCTION

1. QUANTUM ELECTRONICS

A simple technique to compensate the change in phase-matching angle with temperature in critically phase-matched harmonic generation is described. Experimental results are presented for beta barium borate with a nearly a fourfold increase in temperature acceptance bandwidth.

2. ELECTRO-OPTICAL MATERIALS AND DEVICES

The phase-noise characteristics of a harmonically mode-locked fiber laser have been investigated using a new measurement technique called phase-encoded optical sampling. The technique provides 60-dB suppression of amplitude-jitter noise, allowing supermode phase noise to be observed and quantified, and the white-noise pulse-to-pulse timing jitter and rms supermode timing jitter are measured to be less than 50 and 70 fs, respectively.

An analytical model has been developed to predict the evolution of two-dimensional surface profiles in mass transport. Formulated in cylindrical coordinates, the model is potentially useful in practical fabrication of microoptical structures.

3. SUBMICROMETER TECHNOLOGY

An ultraviolet microscope, operating at a 193-nm wavelength, has been constructed using a Schwarzschild-type optical system and an rf microdischarge lamp as the light source. Many materials have absorption edges in this wavelength region leading to large differences in optical properties among materials and thus to increased contrast, allowing the imaging of organic films as thin as 1 nm.

A test bed has been developed to study the competing effects of contamination and cleaning that are present in a 157-nm-wavelength optical system. Hydrocarbon residues are shown to contaminate optical surfaces, but the deposits can be cleaned with the addition of oxygen to the chamber.

4. BIOSENSOR AND MOLECULAR TECHNOLOGIES

Appropriate micron-sized particle simulants for bacteria have been produced and tested to assist the development of a fieldable CANARY (Cellular Analysis and Notification of Antigen Risks and Yields) sensor. These simulant particles stimulate photon emission from B cells, and initial experiments using phosphoryl choline/streptavidin-coated superparamagnetic beads provide information about the potential sensitivity and response time of the CANARY sensor in realistic formats.

5. ADVANCED IMAGING TECHNOLOGY

A 32-by-32-pixel laser radar focal plane array based on Geiger-mode avalanche photodiodes bonded to CMOS digital timing circuits has been fabricated and, to our knowledge, is the first device of its kind. Preliminary experiments verifying the functionality of the device are presented.

6. ANALOG DEVICE TECHNOLOGY

Intermodulation distortion (IMD) has been measured in YBCO bicrystal grain boundaries. The results support the idea that the low-angle grain boundaries in epitaxial films are not the source of the IMD.

7. ADVANCED SILICON TECHNOLOGY

A new effort has been undertaken to scale the metal layers of Lincoln Laboratory's CMOS fabrication process to smaller dimensions. This back-end scaling will significantly improve the density, speed, and power of our 0.18- μm integrated circuits.

REPORTS ON SOLID STATE RESEARCH

1 AUGUST THROUGH 31 OCTOBER 2000

PUBLICATIONS

Electron Cyclotron Resonance Plasma Etching of GaSb-Based Alloys	R. U. Ahmad* G. Nagy* R. M. Osgood, Jr.* G. W. Turner M. J. Manfra J. W. Chludzinski	<i>Appl. Phys. Lett.</i> 77 , 1008 (2000)
High-Frequency Characterization of Sub-0.25- μ m Fully Depleted Silicon-on-Insulator MOSFETs	C-L. Chen R. H. Mathews J. A. Burns P. W. Wyatt D-R. Yost C. K. Chen M. Fritze J. M. Knecht V. Suntharalingam A. M. Soares C. L. Keast	<i>IEEE Electron Device Lett.</i> 21 , 497 (2000)
Resonant-Tunneling-Diode Relaxation Oscillator	C-L. Chen R. H. Mathews L. J. Mahoney S. D. Calawa J. P. Sage K. M. Molvar C. D. Parker P. A. Maki T. C. L. G. Sollner	<i>Solid-State Electron.</i> 44 , 1853 (2000)

*Author not at Lincoln Laboratory.

Electron Beam and Optical Depth
Profiling of Quasibulk GaN

L. Chernyak*
A. Osinsky*
G. Nootz*
A. Schulte*
J. Jasinski*
M. Benamara*
Z. Liliental-Weber*
D. C. Look*
R. J. Molnar

Appl. Phys. Lett. **77**, 2695
(2000)

All-Active InGaAsP-InP Optical
Tapered-Amplifier $1 \times N$ Power
Splitters

S. S. Choi
J. P. Donnelly
S. H. Groves
R. E. Reeder
R. J. Bailey
P. J. Taylor
A. Napoleone
W. D. Goodhue

IEEE Photon. Technol. Lett.
12, 974 (2000)

High Spatial Resolution Thermal
Conductivity and Raman
Spectroscopy Investigation of
Hydride Vapor Phase Epitaxy
Grown *n*-GaN/Sapphire (0001):
Doping Independence

D. I. Florescu*
V. M. Asnin*
F. H. Pollak*
R. J. Molnar
C. E. C. Wood*

J. Appl. Phys. **88**, 3295 (2000)

Nature of the Highly Conducting
Interfacial Layer in GaN Films

J. W. P. Hsu*
D. V. Lang*
S. Richter*
R. N. Kleiman*
A. M. Sergent*
R. J. Molnar

Appl. Phys. Lett. **77**, 2873
(2000)

*Author not at Lincoln Laboratory.

High-Mobility AlGaIn/GaN
Heterostructures Grown by
Molecular-Beam Epitaxy on
GaN Templates Prepared by
Hydride Vapor Phase Epitaxy

M. J. Manfra*
L. N. Pfeiffer*
K. W. West*
H. L. Stormer*
K. W. Baldwin*
J. W. P. Hsu*
D. V. Lang*
R. J. Molnar

Appl. Phys. Lett. **77**, 2888
(2000)

Dual-Band Infrared
Metallodielectric Photonic
Crystal Filters

J. A. Oswald*
B-I. Wu*
K. A. McIntosh
L. J. Mahoney
S. Verghese

Appl. Phys. Lett. **77**, 2098
(2000)

Visualizing Interfacial Structure
at Non-Common-Atom
Heterojunctions with
Cross-Sectional Scanning
Tunneling Microscopy

J. Steinshnider*
M. Weimer*
R. Kaspi*
G. W. Turner

Phys. Rev. Lett. **85**, 2953 (2000)

Phase-Encoded Optical Sampling
for Analog-to-Digital Converters

J. C. Twichell
R. Helkey

IEEE Photon. Technol. Lett.
12, 1237 (2000)

Diode-Pumped 214.8-nm Nd:YAG/
Cr⁴⁺:YAG Microchip Laser
System for the Detection of NO

J. Wormhoudt*
J. H. Shorter*
J. J. Zayhowski

Appl. Opt. **39**, 4418 (2000)

Analysis of Photonic Crystal
Filters by the Finite-Difference
Time-Domain Technique

B-I. Wu*
E. Yang*
J. A. Kong*
J. A. Oswald*
K. A. McIntosh
L. J. Mahoney
S. Verghese

Microw. Opt. Technol. Lett. **27**,
81 (2000)

*Author not at Lincoln Laboratory.

Passively Q -Switched 214.8-nm
Nd:YAG/Cr⁴⁺:YAG Microchip-
Laser System for the Detection
of NO

J. J. Zayhowski
C. C. Cook
J. Wormhoudt*
J. Shorter*

*OSA Trends in Optics and
Photonics*, Vol. 34, *Advanced
Solid State Lasers*, U. Keller,
H. Injeyan, and C. Marshall,
eds. (Optical Society of
America, Washington, D.C.,
2000), p. 409

Miniature Sources of
Subnanosecond 1.4-4.3- μ m
Pulses with High Peak Power

J. J. Zayhowski
A. L. Wilson

*OSA Trends in Optics and
Photonics*, Vol. 34, *Advanced
Solid State Lasers*, U. Keller,
H. Injeyan, and C. Marshall,
eds. (Optical Society of
America, Washington, D.C.,
2000), p. 308

ACCEPTED FOR PUBLICATION

Photon Recycling and
Recombination Processes
in 0.53 eV p -type InGaAsSb

J. M. Borrego*
S. Saroop*
R. J. Gutmann*
G. W. Charache*
T. Donovan*
P. F. Baldasaro*
C. A. Wang

J. Appl. Phys.

Photogenerated Carrier Dynamics
in Epitaxial Lateral Overgrown
GaN

G. E. Bunea*
G. Ulu*
M. S. Ünlü*
B. B. Goldberg*
R. J. Molnar

Phys. Rev. B

*Author not at Lincoln Laboratory.

Polymer Photochemistry at Advanced Optical Wavelengths	T. H. Fedynyshyn R. R. Kunz R. Sinta R. B. Goodman S. P. Doran	<i>J. Vac. Sci. Technol. B</i>
Magic Mobility in Highly Dislocated GaN	D. C. Look* G. E. Stutz* K. Saarinen* R. J. Molnar	<i>Phys. Rev. Lett.</i>
Ultraviolet Photon Counting with GaN Avalanche Diodes	K. A. McIntosh R. J. Molnar L. J. Mahoney K. M. Molvar S. Verghese	<i>Appl. Phys. Lett.</i>
Dual-Band Infrared Metallo- dielectric Photonic Crystal Filters	J. A. Oswald* B-I. Wu* K. A. McIntosh L. J. Mahoney S. Verghese	<i>Appl. Phys. Lett.</i>
Patterning of Sub-50-nm Dense Features with Space-Invariant 157-nm Interference Lithography	M. Switkes M. Rothschild T. M. Bloomstein	<i>Appl. Phys. Lett.</i>
Investigation of Defects in GaN by Photo-electrochemical and Hot Wet Etching	P. Visconti* K. M. Jones* M. A. Reshchikov* R. Cingolani* H. Morkoç* R. J. Molnar	<i>Appl. Phys. Lett.</i>
Evolution of Surface Structure and Phase Separation in GaInAsSb	C. A. Wang R. Calawa C. J. Vineis	<i>J. Cryst. Growth</i>

*Author not at Lincoln Laboratory.

PRESENTATIONS[†]

UV Cleaning of Contaminated Reticles	T. M. Bloomstein V. Liberman M. Rothschild D. E. Hardy	157-nm Reticle Handling Meeting, Vancouver, British Columbia, 1 August 2000
Influence of Jahn-Teller Ions on Spin-Lattice Relaxation in Ferrimagnets	G. F. Dionne	15th International Jahn-Teller Symposium, Boston, Massachusetts, 16-22 August 2000
Minimization of Mask Transmission Asymmetry Effects for Strong Phase-Shift Masks	M. Fritze	20th Annual BACUS Symposium on Photomask Technology, Monterey, California, 13-15 September 2000
A "T" Flipflop Circuit, Operational up to 160 GHz Using Submicron, 20 kA/cm ² , Nb/AlO _x /Al/Nb Josephson Junctions Fabricated with All-Optical Lithography	K. Berggren	Applied Superconductivity Conference, Virginia Beach, Virginia, 17-22 September 2000
Intermodulation Distortion and Josephson Vortices in YBCO Bicrystal Grain Boundaries	D. Oates	Applied Superconductivity Conference, Virginia Beach, Virginia, 17-22 September 2000
Nonlinear Microwave Response of YBaCuO Films of Varying Oxygen Content Before and After Patterning	D. Oates	Applied Superconductivity Conference, Virginia Beach, Virginia, 17-22 September 2000

[†] Titles of presentations are listed for information only. No copies are available for distribution.

Superconducting Filters with
Magnetic Tuning

D. Oates

Applied Superconductivity
Conference,
Virginia Beach, Virginia,
17-22 September 2000

Microwave Ferrites for Low
Temperature Applications

G. F. Dionne

8th International Conference on
Ferrites,
Kyoto, Japan,
18-21 September 2000

Wavelength Beam Combining of
Laser Arrays

T. Y. Fan
A. Sanchez
V. Daneu
A. Goyal
R. Aggarwal
S. C. Buchter
H. K. Choi
G. W. Turner
C. C. Cook

Center for Nonlinear
Optical Materials,
Stanford University,
Stanford, California,
29-30 September 2000

An SOI Based Three-Dimensional
Integrated Circuit Technology

J. A. Burns
L. McIlrath*
J. Hopwood*
C. Keast
D. P. Vu*
K. Warner
P. W. Wyatt

2000 IEEE International SOI
Conference,
Wakefield, Massachusetts,
2-5 October 2000

SLOTFET Fabrication of Self-
Aligned Sub-100-nm Fully-
Depleted SOI CMOS

C. K. Chen
C. L. Keast
P. W. Wyatt
C-L. Chen
J. A. Burns
P. M. Gouker
D. R. Yost
V. Suntharalingam

2000 IEEE International SOI
Conference,
Wakefield, Massachusetts,
2-5 October 2000

*Author not at Lincoln Laboratory.

SOI Wafer Selection for CCD/ SOI-CMOS Technology	V. Suntharalingam B. Burke M. Cooper C. Keast C. K. Chen	2000 IEEE International SOI Conference, Wakefield, Massachusetts, 2-5 October 2000
Polymer Photochemistry at Three Advanced Optical Wavelengths	T. H. Fedynyshyn R. R. Kunz R. F. Sinta R. B. Goodman S. P. Doran	12th International Conference on Photopolymers, McFee, New Jersey, 16-18 October 2000
Quantum Computing with Superconductive Devices	K. Berggren	Quantum Computing for Physical Modeling, North Falmouth, Massachusetts, 18-19 October 2000
Temperature Dependence of the Breakdown Voltage for Reverse- Biased GaN p - n - n^+ Photodiodes	R. L. Aggarwal	Symposium on Spectroscopy of Semiconductors, Purdue University, Lafayette, Indiana, 21 October 2000
An Integrated Superconductive Device Technology for Qubit Control	K. Berggren	Quantum Information Science and Technology, Greenbelt, Maryland, 23-24 October 2000
Biological Agent Warning Sensor (BAWS)	T. H. Jeys M. T. Languirand N. R. Newbury J. H. Kyung G. S. Rowe A. E. DeCew J. J. Zayhowski R. D. Nagle R. P. Brady A. Sanchez	1st Joint Conference on Point Detection for Chemical and Biological Defense, Williamsburg, Virginia, 23-27 October 2000

Placement of Biological Agent
Detectors for Optimum
Performance

T. H. Jeys
J. R. Ochoa

1st Joint Conference on Point
Detection for Chemical and
Biological Defense,
Williamsburg, Virginia,
23-27 October 2000

ORGANIZATION

SOLID STATE DIVISION

D. C. Shaver, *Head*
R. W. Ralston, *Associate Head*
N. L. DeMeo, Jr., *Assistant*
Z. J. Lemnios, *Senior Staff*

J. W. Caunt, *Assistant Staff*
K. J. Challberg, *Administrative Staff*
J. D. Pendergast, *Administrative Staff*

SUBMICROMETER TECHNOLOGY

M. Rothschild, *Leader*
T. M. Lyszczarz, *Assistant Leader*
T. H. Fedynyshyn, *Senior Staff*
R. R. Kunz, *Senior Staff*

Astolfi, D. K.	Liberman, V.
Bloomstein, T. M.	Maki, P. A.
DiNatale, W. F.	Mowers, W. A.
Doran, S. P.	Palmacci, S. T.
Efremow, N. N., Jr.	Sedlacek, J. H. C.
Forte, A. R.	Spector, S. J.
Geis, M. W.	Switkes, M.
Goodman, R. B.	Sworin, M.
Krohn, K. E.	Uttaro, R. S.

QUANTUM ELECTRONICS

A. Sanchez-Rubio, *Leader*
T. Y. Fan, *Assistant Leader*
T. H. Jeys, *Senior Staff*
J. J. Zayhowski, *Senior Staff*

Aggarwal, R. L.	Goyal, A. K.
Buchter, S. C.	Herzog, W. D.
Daneu, J. L.	Lynch, E. J.
Daneu, V.	O'Brien, P. W.
DiCecca, S.	Ochoa, J. R.

ELECTRO-OPTICAL MATERIALS AND DEVICES

J. C. Twichell, *Leader*
G. W. Turner, *Assistant Leader*
D. L. Spears, *Senior Staff*
R. C. Williamson, *Senior Staff*

Bailey, R. J.	Huang, R. K.	Napoleone, A.
Betts, G. E.	Juodawlkis, P. W.	Nitishin, P. M.
Calawa, D. R.	Liau, Z. L.	Oakley, D. C.
Calawa, S. D.	Mahoney, L. J.	O'Donnell, F. J.
Connors, M. K.	Manfra, M. J.	Plant, J. J.
Donnelly, J. P.	McIntosh, K. A.	Taylor, P. J.
Goodhue, W. D.	Missaggia, L. J.	Walpole, J. N.
Hargreaves, J. J.	Molnar, R. J.	Wang, C. A.
Harman, T. C.	Mull, D. E.	Younger, R. D.
Harris, C. T.		

*Part Time

BIOSENSOR AND MOLECULAR
TECHNOLOGIES

M. A. Hollis, *Leader*

Blanchard, D. J.	Nargi, F. E.
Graves, C. A.	Parameswaran, L.
Harper, J. D.	Petrovick, M. S.
Mathews, R. H.	Rider, T. H.

ANALOG DEVICE TECHNOLOGY

T. C. L. G. Sollner, *Leader*
L. M. Johnson, *Assistant Leader*
A. C. Anderson, *Senior Staff*

Anthony, M. P.	Murphy, P. G.
Berggren, K. K.	Oates, D. E.
Boisvert, R. R.	Sage, J. P.
Fitch, G. L.	Santiago, D. D.
Holtham, J. H.	Seaver, M. M.
Kohler, E. J.	Slattery, R. L.
Lyons, W. G.	Weir, T. J.
Macedo, E. M., Jr.	

ADVANCED IMAGING TECHNOLOGY

B. B. Kosicki, *Leader*
R. K. Reich, *Assistant Leader*
B. E. Burke, *Senior Staff*

Aull, B. F.	Johnson, K. F.
Ciampi, J. S.	Lind, T. A.
Cooper, M. J.	Loomis, A. H.
Craig, D. M.	McGonagle, W. H.
Daniels, P. J.	O'Mara, D. M.
Doherty, C. L., Jr.	Percival, K. A.
Dolat, V. S.	Rathman, D. D.
Felton, B. J.	Stern, A.
Gregory, J. A.	Young, D. J.

ADVANCED SILICON TECHNOLOGY

C. L. Keast, *Leader*
P. W. Wyatt, *Associate Leader*

Austin, E. E.	Knecht, J. M.
Berger, R.	Newcomb, K. L.
Bozler, C. O.	Rabe, S.
Burns, J. A.	Soares, A. M.
Chen, C. K.	Suntharalingam, V.
Chen, C. L.	Travis, L.
Davis, P. V.	Tyrrell, B. M.
D'Onofrio, R. P.	Warner, K.
Fritze, M.	Yost, D.-R.
Gouker, P. M.	Young, G. R.

1. QUANTUM ELECTRONICS

1.1 PASSIVE TEMPERATURE COMPENSATION IN CRITICALLY PHASE-MATCHED HARMONIC GENERATION

In laser systems that are to be operated in the field as opposed to a laboratory, it is desirable to reduce the number of parameters requiring active control to a minimum. Many commonly used nonlinear optical materials require that the ambient temperature be maintained within a narrow range to ensure optimized conversion of the input radiation. As an alternative, the crystal's angular orientation can be changed, but this too requires active control. We present a simple means of passively compensating temperature changes using only a prism. Compensation of the resulting beam pointing can be achieved with a second prism after the nonlinear crystal. As an example, we present experimental results of frequency doubling 532-nm light to 266 nm in beta barium borate (BBO).

The basic concept is illustrated in Figure 1-1. Radiation to be converted enters the prism first and is deflected by an angle dependent on the index of refraction, angle of incidence, apex angle, and temperature. By a proper choice of prism material and geometry, this temperature-dependent deflection $d(T)$ can be used to track the temperature dependence of the phase-matching angle $\theta(T)$ in a nonlinear material. Here, $d(T)$ is given by

$$d(T) = \phi + \sin^{-1} \left[n(T) \left(\sin \left(\beta - \left(\sin^{-1} (\sin(\phi)/n(T)) \right) \right) \right) \right] - \beta \quad (1.1)$$

where ϕ is the input prism angle, β is the prism apex angle, and $n(T)$ is the index of refraction as a function of temperature for the prism. If $\theta(T)$ is known for a given nonlinear material, these three parameters can be chosen such that phase matching is maintained over a much wider temperature range than would be possible otherwise. The resulting beam pointing, which may be undesirable, can be compensated in a similar manner with a prism after the nonlinear crystal, optimized for the output wavelength. By a suitable choice of beam diameter in the second prism, beam translation can be reduced to a small fraction of the beam width.

As an experimental demonstration, we chose to frequency double 532-nm light in BBO. The source was a passively Q -switched microchip laser operating at 1064 nm which was doubled in KTP to provide radiation at 532 nm [1]. The prism was made of fused silica with an apex angle β of 60°. By using values from [2] and [3], the phase-matching angle as a function of temperature $\theta(T)$, along with the temperature dependent deflection $d(T)$ from the prism, was calculated for various incidence angles. The optimum input angle for compensation was found to be 30.7 degrees when considering only first-order temperature derivatives. Figure 1-2 shows the difference between the phase-matching angle change and the prism deflection angle for three incident angles. This calculation indicates that alignment errors of ± 1 degree

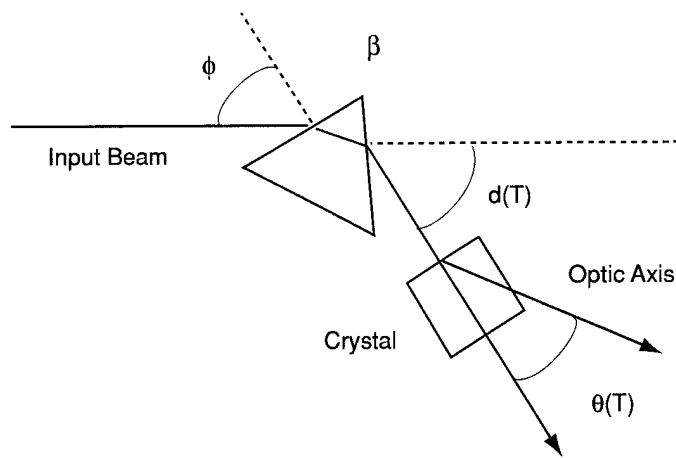


Figure 1-1. Diagram of passive temperature compensation concept.

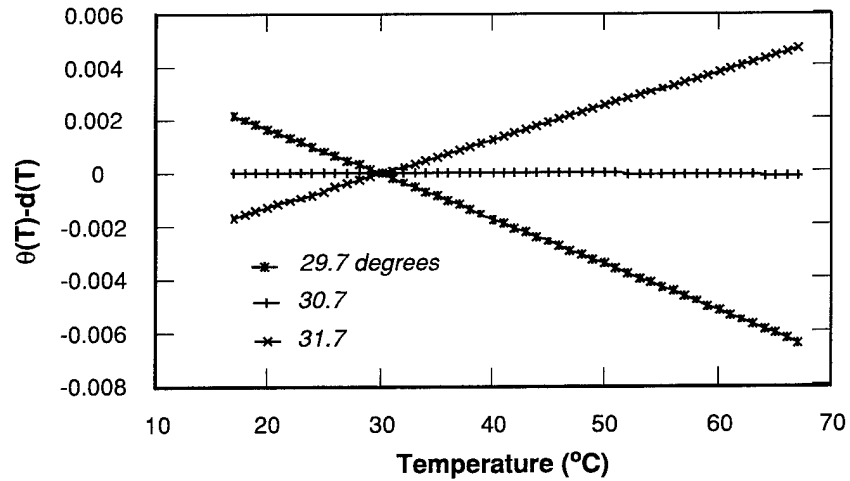


Figure 1-2. Difference between $\theta(T)$ and $d(T)$ for three incidence angles on the prism.

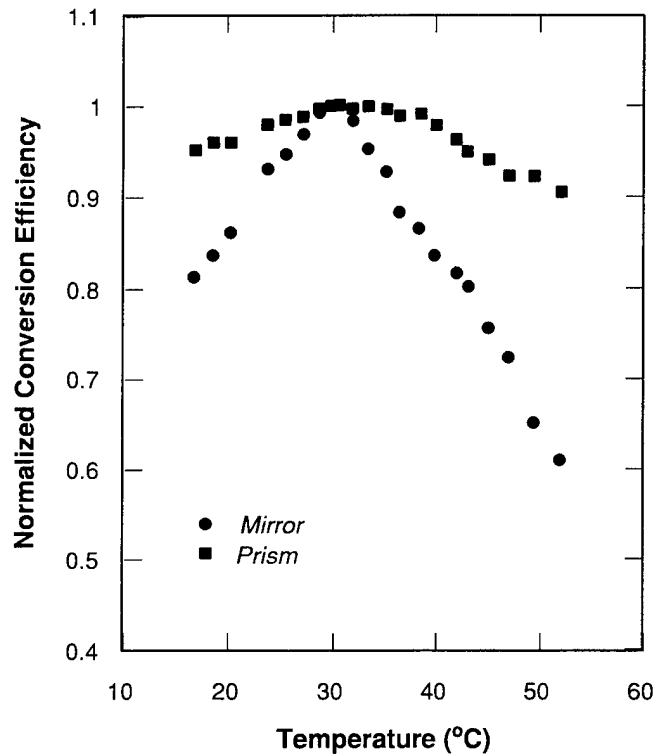


Figure 1-3. Experimental conversion efficiencies for compensated and uncompensated harmonic generation.

should have only a small effect on conversion efficiency as the plane-wave acceptance angle for this interaction in BBO is ~ 0.02 degree-cm. The prism and 7-mm BBO crystal were mounted on a common copper base in a temperature-controlled oven. The input 532-nm beam was loosely focused and directed through the prism at an incident angle of ~ 30.7 degrees. This resulted in a beam diameter of $\sim 100 \mu\text{m}$ over the length of the BBO. The prism could be replaced by a flat mirror to provide a side-by-side comparison of the temperature compensation. The temperature was set at 30°C and phase matching was then optimized for 266-nm generation. The temperature was ramped up and down over the range $T = 17\text{--}52^\circ\text{C}$ with no further mechanical adjustments. The normalized conversion efficiencies for the case of prism and mirror are shown in Figure 1-3. As can be seen from Figure 1-3, complete compensation was not achieved despite the fact that Figure 1-2 indicates nearly perfect compensation should be possible. The cause of this discrepancy can be attributed to a number of factors in our nonoptimized experimental arrangement. First, owing to the geometry of our oven, it was not possible to operate at precisely 30.7 degrees. The angle was greater by roughly 0.5 degree. Second, the expansion and contraction of the copper base plate may have resulted in slight, unpredictable twists of the prism and BBO with respect to each other. Using a base made of Invar or similar low thermal expansion material should improve this. Third, published values for the

temperature derivatives of the refractive indices in both materials are given only to first order. At some point the second- and higher-order terms may limit the maximum temperature range for which compensation is possible.

In conclusion, we have demonstrated a simple way to passively compensate the phase-matching angle change in critically phase-matched harmonic generation. With a simple, nonoptimized experimental setup we have shown nearly a fourfold increase in the 90% conversion efficiency bandwidth in BBO. This method is not unique to this crystal. Geometries and prism materials can provide compensation with other nonlinear crystals as well.

S. C. Buchter

P. W. O'Brien

REFERENCES

1. J. J. Zayhowski, *Rev. Laser Eng.* **26**, 841 (1998).
2. K. Kato, *IEEE J. Quantum Electron.* **22**, 1013 (1986).
3. J. H. Wray and J. T. New, *J. Opt. Soc. Am.* **59**, 774 (1969).

2. ELECTRO-OPTICAL MATERIALS AND DEVICES

2.1 MEASUREMENT OF MODE-LOCKED LASER TIMING JITTER USING PHASE-ENCODED OPTICAL SAMPLING

Actively mode-locked lasers producing trains of picosecond pulses are becoming increasingly important in applications such as photonic analog-to-digital (A/D) converters and ultrafast optical communications. The timing and amplitude jitter of these mode-locked laser sources can limit system performance. A number of studies have been performed to understand and reduce the various jitter mechanisms [1]–[4]. The time scales of these jitter mechanisms vary from pulse-to-pulse fluctuations to long-term drifts, and the relevant time scale is strongly application dependent. The photonic A/D converter application has a very stringent jitter requirement. To sample a 3-GHz signal with 12-bit resolution (74-dB signal-to-noise ratio), the laser's rms pulse-to-pulse timing jitter must be less than 10 fs. Here, we report on the use of phase-encoded optical sampling [5] to measure the pulse-to-pulse and pattern-noise timing jitter of a harmonically mode-locked fiber laser. This interferometric technique suppresses the amplitude noise by 60 dB, allowing the laser's phase noise to be independently measured. The pulse-to-pulse timing jitter and the harmonic pattern-noise timing jitter of the laser are less than 50 and 70 fs, respectively.

Methods used to measure mode-locked laser noise include rf spectral analysis of the detected laser output [1]–[3], and optical cross-correlation [4]. The spectral analysis techniques integrate many pulses to estimate the laser's phase-noise spectral density. An effective rms timing jitter can then be derived by integrating the spectral density over a specific frequency range. Pulse-to-pulse jitter estimates require integration out to the laser repetition frequency and are often limited by the maximum offset frequency or the noise floor of the spectrum analyzer. In a typical optical cross-correlation measurement, the timing jitter is estimated by measuring the cross-correlation width as a function of integral pulse delay.

Harmonically mode-locked lasers also generate correlated supermode or pattern noise that is periodic at the fundamental cavity frequency [6]. In a photonic A/D converter, this pattern noise produces a periodic sampling error that reduces the spur-free dynamic range of the converter.

Phase-encoded sampling uses the periodic optical pulse train generated by a mode-locked laser to sample an electrical signal via an electro-optic modulator. By sampling a low-noise sinusoid, deviations between the sampled sinusoid and the input sinusoid can be related to the amplitude and timing jitter of the mode-locked laser. In the following analysis, we consider only the effects of laser timing jitter since the phase-encoded sampling technique is insensitive to laser amplitude noise (see discussion of Figure 2-2 below). The analysis is also restricted to timing jitter with a stationary or cyclostationary white-noise distribution, and low-frequency phase noise is neglected.

Consider an optical pulse source consisting of a laser mode locked at the N th harmonic of the fundamental cavity frequency. Ideally, the pulses in the laser would be equally spaced at intervals of T/N , where T is the cavity round-trip time. In an actual laser, the N -pulse pattern contains timing variations

resulting from reference oscillator noise, mismatch between the reference frequency and the cavity length, and spontaneous emission noise. Depending on the laser dynamics, the timing jitter pattern may change rapidly or evolve slowly over a number of round-trips.

If the pattern timing jitter distribution is uncorrelated from round-trip to round-trip, the timing jitter contributes to only the white noise of the sampled signal. This case is identical to the timing jitter of a fundamentally mode-locked laser, and the pulse-to-pulse timing jitter can be estimated from the signal-to-jitter-noise ratio $(S/N)_{\text{JITTER}}$ of the sampled signal. When an input sinusoid is sampled at points of uniformly distributed phase, the variance of the timing jitter in the Nyquist bandwidth is

$$\sigma_{\tau}^2 = \frac{1}{4\pi^2 f_0^2 \left(\frac{S}{N}\right)_{\text{JITTER}}} = \frac{1}{4\pi^2 f_0^2 \frac{P_s}{(P_N - P_Q)}} \quad (2.1)$$

where f_0 and P_s are the frequency and power of the sampled sinusoid, P_N is the total white-noise power in the Nyquist bandwidth, and P_Q is the non-jitter white-noise power in the optical sampling system (e.g., quantization noise, thermal noise, shot noise).

Alternatively, if the pattern timing jitter distribution is completely correlated from round-trip to round-trip (i.e., N -pulse jitter pattern never changes), the optical sampling clock contains an error component that is periodic at the laser round-trip frequency f_R . This periodic error creates sideband spurs at frequencies $f_k = f_0 + kf_R$, where $k = \pm 1, \pm 2, \dots$. All of the sampling noise is contained in these sidebands, and the white-noise floor is unaffected. For this case, with f_0 much greater than the sampling frequency, the rms value of the fixed timing jitter pattern is

$$\sigma_{\tau}^2 = \frac{N}{4\pi^2 f_0^2 \langle \text{SASR} \rangle} \quad (2.2)$$

where $\langle \text{SASR} \rangle$ is the signal-to-average-spur ratio. To be exact, $\langle \text{SASR} \rangle$ is an ensemble average over a set of random jitter patterns with variance σ_{τ}^2 . We approximate $\langle \text{SASR} \rangle$ as the ratio of the signal power to the average power in the pattern-noise spurs in a single power spectrum.

In general, the timing jitter pattern of a harmonically mode-locked laser will be partially correlated. The spectral width of the pattern-noise sidebands will be inversely related to the correlation time. The calculated $\langle \text{SASR} \rangle$ in Equation (2.2) must account for this by spectrally integrating the total power in each spur.

The polarization-maintaining, Er-fiber ring laser characterized here serves as the short-pulse sampling clock in the phase-encoded optical sampling system, shown in Figure 2-1. Harmonic mode locking is accomplished by driving an intracavity LiNbO₃ Mach-Zehnder (MZ) amplitude modulator with

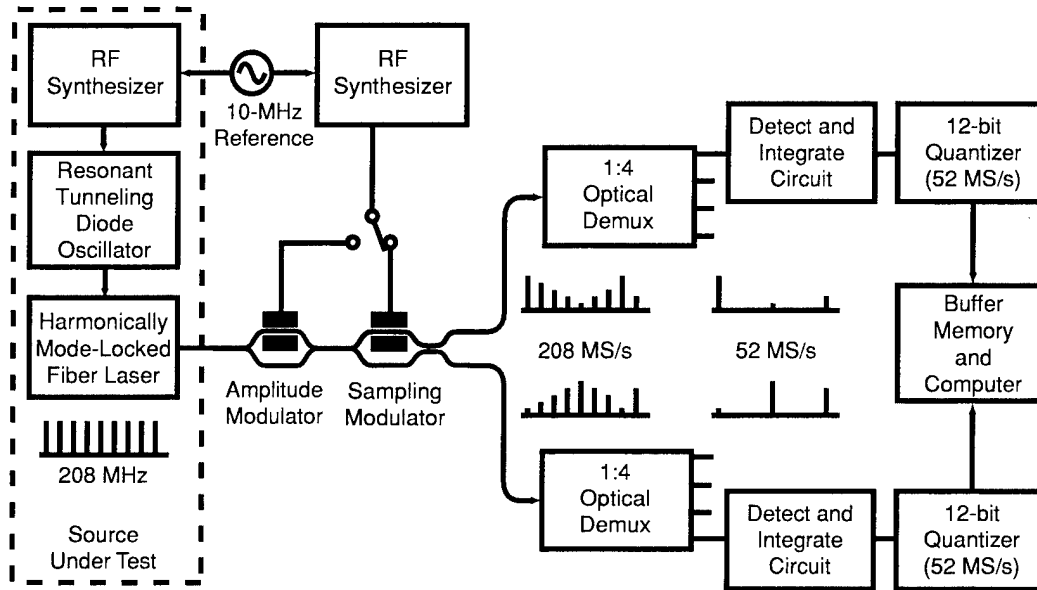


Figure 2-1. Phase-encoded optical sampling system consisting of harmonically mode-locked fiber laser, 1:4 optical time-division demultiplexers, detect and integrate circuits, 12-bit quantizers (AD6640), buffer memory, and computer control. The additional amplitude modulator is included to investigate laser-amplitude-noise suppression.

180-ps electrical pulses produced by a resonant tunneling diode (RTD) oscillator [7]. Use of the short RTD oscillator pulses allows the laser to generate 30-ps pulses at a relatively low 208-MHz repetition rate (21st cavity harmonic). The RTD oscillator is injection locked at its 23rd harmonic (4.78 GHz) using an HP8665B synthesizer. Although no active cavity stabilization was used for our measurements, excellent side-mode suppression (>65 dB) was observed when the cavity length was matched to the RTD oscillator frequency.

The laser pulses are used to sample an electrical signal applied to a dual-output LiNbO_3 MZ interferometer with a 3-GHz bandwidth. The modulated pulse trains from both MZ outputs are rate-reduced to 52 MHz using a pair of 1:4 time demultiplexers, detected, and quantized with two 12-bit A/D converters. A highly linear estimate of the sampled RF voltage is obtained by combining the complementary output samples and digitally inverting the MZ transfer function, a process referred to as phase decoding [5]. Below, we refer to the case where only one output of the MZ is used as intensity sampling.

The amplitude noise suppression was determined by amplitude modulating the laser pulse train with a 3-GHz sinusoid before injecting it into the sampling modulator. The fast Fourier transform (FFT) power spectra in Figure 2-2 reveal that the normalization inherent in the phase-encoded sampling technique

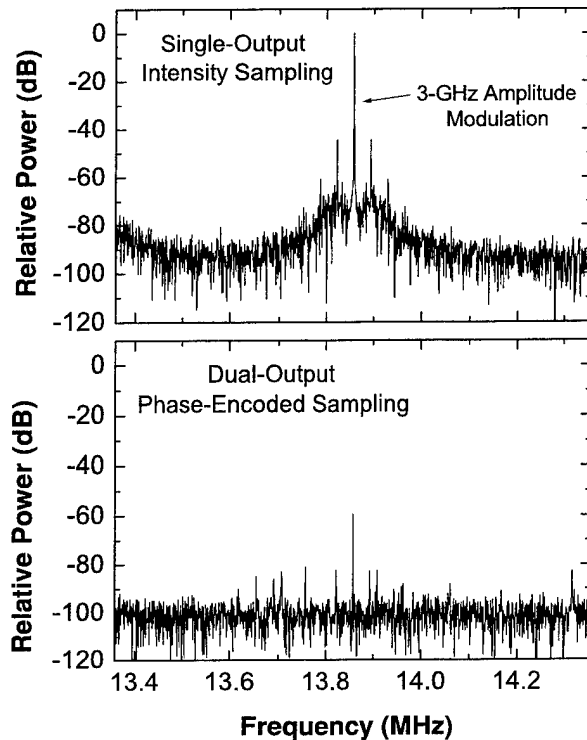


Figure 2-2. Power spectra of optically sampled data with artificially induced laser amplitude noise: intensity sampling (top) and phase-encoded sampling (bottom). Amplitude-noise suppression due to phase-encoded sampling is 60 dB. The 3-GHz amplitude modulation “noise” signal aliases to 13.86 MHz for the sampling rate of 52 MS/s.

reduces the magnitude of the amplitude modulation by 60 dB. The intensity-sampled spectrum, shown in Figure 2-2 (top), also contains typical fiber laser relaxation-oscillation sidebands with a peak at 35-kHz offset frequency. Most of the relaxation-oscillation energy is amplitude noise since it is suppressed in the phase-decoded spectrum, shown in Figure 2-2 (bottom). However, the narrow sidebands at 35-kHz offset are suppressed by only 30 dB, indicating the presence of a phase-noise component.

The pulse-to-pulse and pattern timing jitter were investigated by sampling a 3-GHz sinusoid with $P_S = +13.6$ dBm. The spectrum of the phase-decoded signal, shown in Figure 2-3 (top), contains the aliased 3-GHz tone and its harmonics, a raised noise floor, and a set of pattern-noise spurs. To accentuate the pattern-noise spurs, the cavity length was detuned slightly, causing the side-mode suppression ratio to decrease from >65 to 50 dB. Frequency spacing of the pattern-noise spurs is reduced from f_R to $f_R/4$ (2.475 MHz) by the 1:4 time demultiplexers.

With no signal applied, as seen in Figure 2-3 (bottom), the pattern-noise spurs are not present and the noise floor decreases by 3.7 dB. Some of the signal-dependent noise floor increase (1.7 dB) can be

attributed to the nonlinear effect of uncorrelated system noise on the phase-decoding process at high modulation depth. Excluding the enhanced system noise, $P_N = 58$ nW and $P_Q = 37$ nW. Substituting into Equation (2.1) yields $\sigma_\tau = 50$ fs. This value is an upper bound since it includes the phase noise of the HP8665B synthesizer used to generate the 3-GHz input sinusoid.

The nature of the timing jitter pattern correlation can be discerned by examining a pattern-noise spur ($k = -3$) for the detuned laser with a narrow frequency scale, as shown in Figure 2-4. The spur spectral width is about 70 kHz, revealing a pattern correlation time on the order of 10–20 μ s. The pattern spur in the intensity-sampled data, seen in Figure 2-4 (top), which contains both amplitude and timing pattern noise, peaks at the calculated spur frequency (dotted line) as expected. However, the pattern timing jitter spur in the phase-encoded sampled data, seen in Figure 2-4 (bottom), has a null at the spur frequency. All the phase-decoded spurs show similar nulls. We attribute this null to a damped oscillation of the pulse around the center of the laser's intracavity modulation window. When the laser cavity length is optimally matched to the harmonic drive frequency, the amplitude of the pattern-noise spurs decreases to a value just above the noise floor (data not shown).

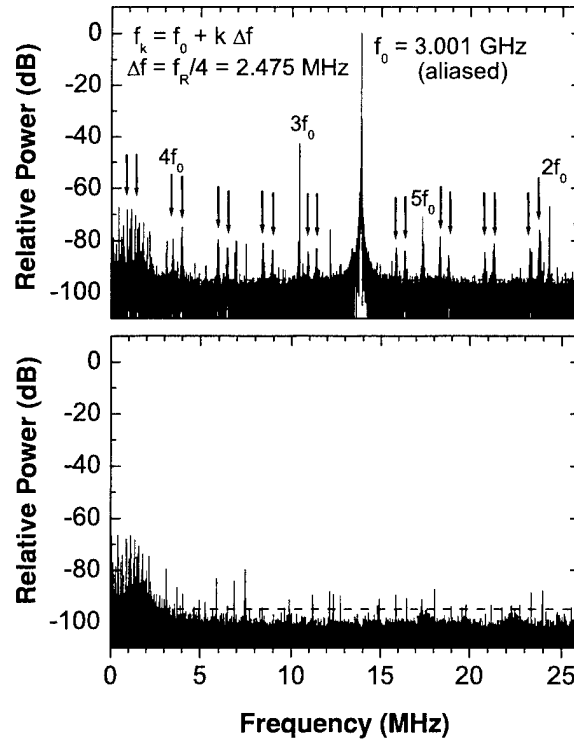


Figure 2-3. Power spectra of optically sampled data for the following inputs: 3-GHz sinusoid (top) and no signal (bottom). Note the noise floor increase (dotted line) and the pattern noise spurs (indicated by arrows) when the sinusoid is present.

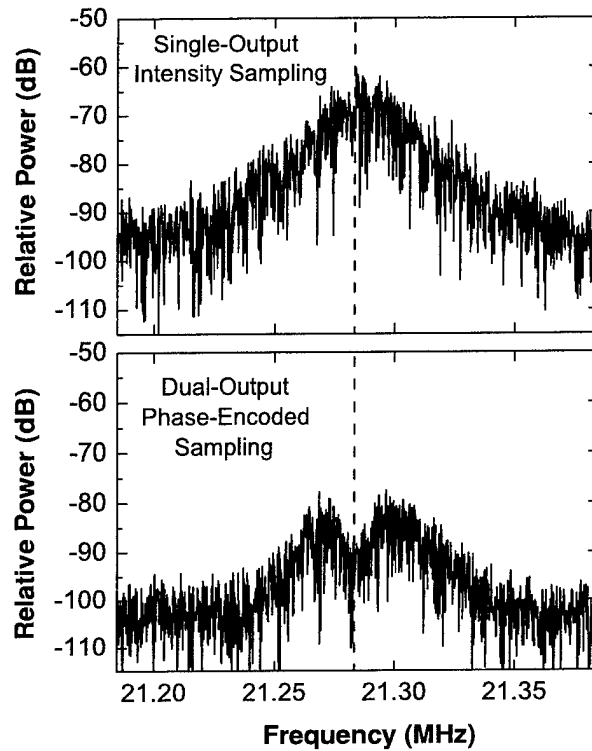


Figure 2-4. Power spectra of individual pattern noise spur for intensity sampling (top) and phase-encoded sampling (bottom). Dotted lines show the calculated frequency of the pattern-noise spur.

The rms value of the pattern timing jitter can be estimated from Equation (2.2) by first integrating the total power of each spur over the spur spectral width, and then calculating the $\langle \text{SASR} \rangle$ from the 20 sideband spurs. By using an integration bandwidth of 100 kHz, $\sigma_t = 250$ and 70 fs for the detuned and optimized laser conditions, respectively. The optimized-laser pattern timing jitter value is an upper bound limited by the noise floor of the current measurement system.

We have demonstrated a new method to measure wideband pulse-to-pulse and correlated pattern (supermode) timing jitter of mode-locked lasers. The 60 dB of amplitude noise suppression in the phase-encoded sampling system is likely limited by residual calibration errors. We have also shown that the short-pulse output of an RTD oscillator can be used to mode lock a fiber laser, producing 30-ps pulses at a 208-MHz rate with <50-fs pulse-to-pulse timing jitter.

P. W. Juodawlkis	J. C. Twichell
J. L. Wasserman	G. E. Betts
R. C. Williamson	

2.2 TWO-DIMENSIONAL MODEL OF SURFACE-ENERGY-INDUCED MASS TRANSPORT IN CYLINDRICAL COORDINATES

Surface energy has been used to transform etched mesas into useful microoptical structures in semiconductor wafers [8]–[11]. This mass-transport process has previously been modeled analytically both in one- and two-dimensional cases [12]–[16]. The previous two-dimensional model [16], however, was based on rectangular coordinates and is not suitable for most applications. In this work, funded under a cooperative research and development agreement (CRDA) with AXSUN Technologies, Inc., a two-dimensional model has been developed in cylindrical coordinates.

As illustrated in Figure 2-5, we first consider a slowly varying surface profile of a Bessel function of order m

$$f(\rho, \phi) = AJ_m(k\rho) \cos m\phi \quad (2.3)$$

More general profiles can be expressed in Fourier-Bessel integrals as will be elaborated later. Since $J_m(k\rho)$ satisfies the Bessel's equation

$$\frac{d^2}{d\rho^2} J_m(k\rho) + \frac{1}{\rho} \frac{d}{d\rho} J_m(k\rho) + \left(k^2 - \frac{m^2}{\rho^2} \right) J_m(k\rho) = 0 \quad (2.4)$$

one can readily verify that f is an eigenfunction of the Laplacian operator ∇^2 , i.e.,

$$\begin{aligned} \nabla^2 f &\equiv \left(\frac{\partial^2}{\partial \rho^2} + \frac{1}{\rho} \frac{\partial}{\partial \rho} + \frac{1}{\rho^2} \frac{\partial^2}{\partial \phi^2} \right) f \\ &= -k^2 f \end{aligned} \quad (2.5)$$

For a slowly varying profile, the surface curvature is given by the Laplacian of the profile, and the surface energy is therefore given by [14]–[16]

$$\varepsilon = -\alpha v \nabla^2 f \quad (2.6)$$

where α and v are, respectively, the coefficient of surface tension and the molecular volume of the material. For an eigenfunction profile [Equation (2.5)] the surface energy simplifies to

$$\varepsilon = \alpha v k^2 f \quad (2.7)$$

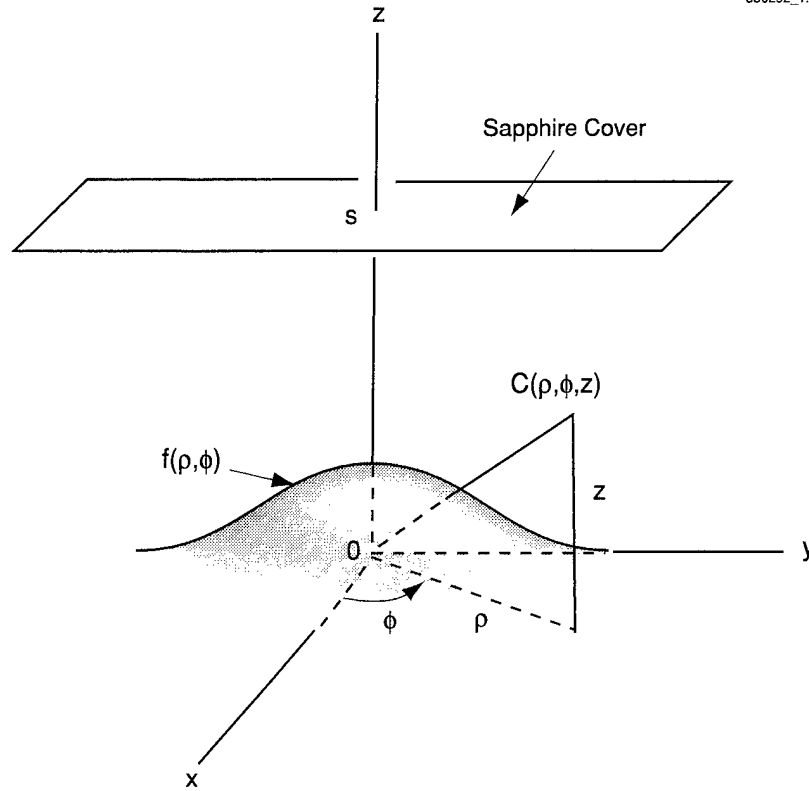


Figure 2-5. Illustration of surface profile and cylindrical coordinates used in this work, where the transformation of the profile due to surface-energy-induced mass transport is considered.

The surface energy represents a decrease in binding energy and increase in surface dissociation. The equilibrium vapor concentration will shift accordingly by the factor $e^{\varepsilon/k_B T}$, where k_B is the Boltzmann constant. (In this work, we consider mass transport via vapor diffusion similar to [15], but the basic concepts are also directly applicable to surface diffusion.) In the parameter ranges of most practical interest, it can readily be shown that $\varepsilon \ll k_B T$, and $e^{\varepsilon/k_B T} \cong [1 + (\varepsilon/k_B T)]$. With the small deviation from equilibrium and the experimentally observed slow mass-transport rates, it is plausible to assume a quasi-equilibrium along the surface, where the vapor concentration is given by

$$C(\rho, \phi, z=0) = C_0 + \frac{C_0}{k_B T} \alpha v k^2 f \quad (2.8)$$

with C_0 being the equilibrium vapor concentration of a flat surface. (Note that the surface profile is assumed to have a small amplitude.)

Now, consider the vapor concentration $C(\rho, \phi, z)$ in the space between the surface ($z = 0$) and the sapphire cover ($z = s$). Conservation of mass requires

$$\nabla^2 C(\rho, \phi, z) = 0$$

or

$$\frac{\partial^2 C}{\partial \rho^2} + \frac{1}{\rho} \frac{\partial C}{\partial \rho} + \frac{1}{\rho^2} \frac{\partial^2 C}{\partial \phi^2} + \frac{\partial^2 C}{\partial z^2} = 0 \quad (2.9)$$

(Strictly speaking, the continuity equation reads $D\nabla^2 C = \partial C / \partial t$, but it can be shown that $\partial C / \partial t$ is negligible.) This linear differential equation can be solved by separation of variables

$$C - C_0 = c(\rho, \phi) Z(z) \quad (2.10)$$

Since c is directly proportional to f [Equation (2.8)], we have from Equation (2.5)

$$\frac{\partial^2 c}{\partial \rho^2} + \frac{1}{\rho} \frac{\partial c}{\partial \rho} + \frac{1}{\rho^2} \frac{\partial^2 c}{\partial \phi^2} = -k^2 c$$

and then Equation (2.9) leads to

$$\frac{d^2 Z}{dz^2} = k^2 Z \quad (2.11)$$

The boundary conditions of $Z(0) = 1$ and $\left. \frac{dZ}{dz} \right|_{z=s} = 0$ then yields

$$Z(z) = \frac{\cosh k(s-z)}{\cosh ks} \quad (2.12)$$

(The vanishing derivative at $z = s$ is required by the absence of a net diffusion flux normal to the sapphire cover.) We therefore have

$$C(\rho, \phi, z) = C_0 + \frac{C_0}{k_B T} \alpha v k^2 f(\rho, \phi) \frac{\cosh k(s-z)}{\cosh ks} \quad (2.13)$$

The time evolution of the surface profile can now be considered. The diffusion flux normal to the wafer surface is given by

$$-D \frac{\partial C}{\partial z} \Big|_{z=0} = \frac{C_0 D}{k_B T} \alpha v k^3 f \tanh ks \quad (2.14)$$

where D is the vapor diffusivity. Conservation of mass then requires a corresponding change in the surface profile

$$-\frac{1}{v} \frac{\partial f}{\partial t} = -D \frac{\partial C}{\partial z} \Big|_{z=0} \quad (2.15)$$

or

$$\frac{\partial f}{\partial t} = - \left(\frac{C_0 D}{k_B T} \alpha v^2 k^3 \tanh ks \right) f \quad (2.16)$$

This means that the amplitude of the eigenfunction f undergoes an exponential decay with a lifetime

$$\tau = \left(\frac{C_0 D}{k_B T} \alpha v^2 k^3 \tanh ks \right)^{-1} \quad (2.17)$$

similar to the previously treated one-dimensional case [15]. Note that τ decreases with an increased s , but reaches a limit, since $\tanh ks \rightarrow 1$. (In practice, a sufficient separation s between the sapphire cover and the wafer can be chosen to maximize the mass transport rate without compromising the wafer protection.) This regime of

$$\tau = (\beta k^3)^{-1} \quad (2.18)$$

where β is a constant will be used in the following discussions.

A more general surface profile can be expanded as a superposition of eigenfunctions in the form of a Fourier-Bessel integral [17]

$$f(\rho, t=0) = \int_0^\infty A(k) J_0(k\rho) dk \quad (2.19)$$

where

$$A(k) = k \int_0^\infty \rho' f(\rho', 0) J_0(k\rho') d\rho' \quad (2.20)$$

and the simpler case of a circularly symmetric profile (i.e., $m = 0$) is considered. The evolution of the profile in mass transport is then given by

$$f(\rho, t) = \int_0^\infty e^{-\beta k^3 t} A(k) J_0(k\rho) dk \quad (2.21)$$

Two cases of practical interest are considered below.

When the starting profile is a narrow mesa, it can be approximated as a δ -function, i.e.,

$$f(\rho, 0) = \delta(\rho) / \rho \quad (2.22)$$

Equation (2.20) with $J_0(0) = 1$ then yields

$$A(k) = k \quad (2.23)$$

and

$$f(\rho, t) = \int_0^\infty e^{-\beta k^3 t} k J_0(k\rho) dk \quad (2.24)$$

By the changes of variables

$$\kappa \equiv (\beta t)^{1/3} k \quad (2.25)$$

and

$$\xi \equiv \rho / (\beta t)^{1/3} \quad (2.26)$$

the above integral can be transformed to

$$\begin{aligned} f(\rho, t) &= \frac{1}{(\beta t)^{2/3}} \int_0^\infty e^{-\kappa^3} \kappa J_0(\kappa \xi) d\kappa \\ &= F(\xi) / (\beta t)^{2/3} \end{aligned} \quad (2.27)$$

Note that the integral is a function of ξ only, and is denoted by $F(\xi)$. This means that the profile maintains a universal shape but expands laterally according to $t^{1/3}$. The function $F(\xi)$ has been evaluated by carrying out the integration numerically and is shown in Figure 2-6.

Another case of practical interest is that of a single cylindrical mesa

$$f(\rho, 0) = \begin{cases} A_0 & \text{for } \rho \leq a \\ 0 & \text{for } \rho > a \end{cases} \quad (2.28)$$

The function $A(k)$ is now given by

$$\begin{aligned} A(k) &= A_0 k \int_0^a \rho' J_0(k\rho') d\rho' \\ &= A_0 a J_1(ka) \end{aligned} \quad (2.29)$$

where the last step can be verified by the series expansion of Bessel functions. We therefore have

$$f(\rho, t) = A_0 a \int_0^\infty e^{-\beta k^3 t} J_1(ka) J_0(k\rho) dk \quad (2.30)$$

This integral has been evaluated numerically for several values of t , as shown in Figure 2-7. The calculated profiles show general agreement with experimental observations, but a more quantitative comparison will be a subject of further investigation.

Z. L. Liao
M. B. Stern*

*Author presently with AXSUN Technologies, Inc., Billerica, Massachusetts.

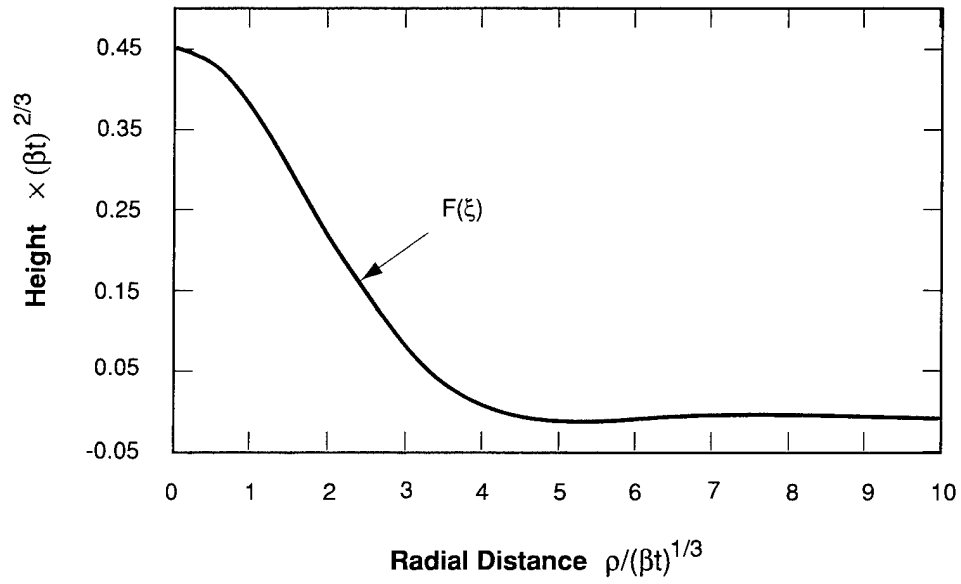


Figure 2-6. Universal profile that characterizes the time evolution of an initial δ -function.

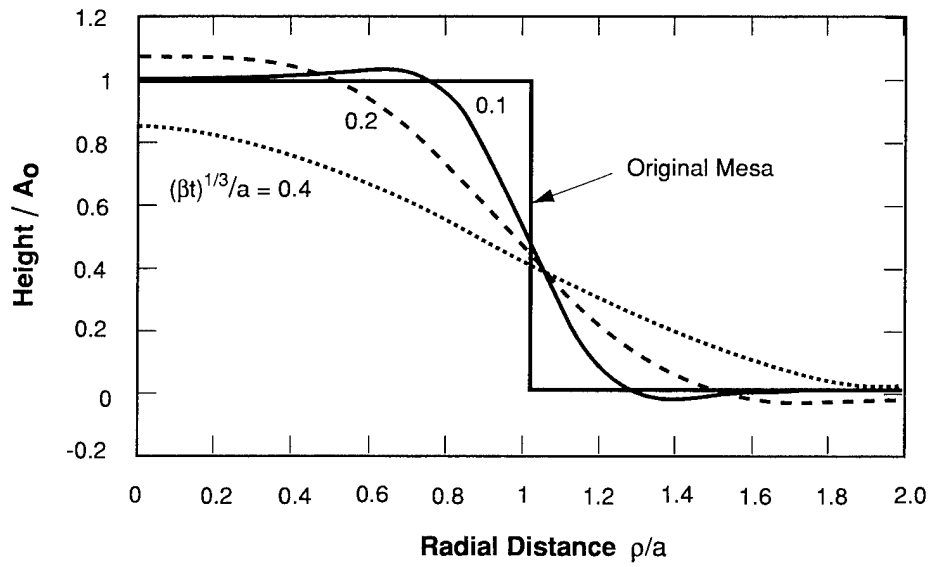


Figure 2-7. Evolution of single cylindrical mesa of radius a and height A_0 as predicted in the present model.

REFERENCES

1. D. von der Linde, *Appl. Phys. B* **39**, 201 (1986).
2. U. Keller, K. D. Li, M. Rodwell, and D. M. Bloom, *IEEE J. Quantum Electron.* **25**, 280 (1989).
3. T. R. Clark, T. F. Carruthers, P. J. Matthews, and I. N. Duling III, *Electron. Lett.* **35**, 720 (1999).
4. K. Tamura and M. Nakazawa, *Opt. Lett.* **23**, 1360 (1998).
5. J. C. Twichell and R. Helkey, *IEEE Photon. Technol. Lett.* **12**, 1237 (2000).
6. M. F. Becker, D. J. Kuizenga, and A. E. Siegman, *IEEE J. Quantum Electron.* **8**, 687 (1972).
7. E. R. Brown, C. D. Parker, S. Verghese, M. W. Geis, and J. F. Harvey, *Appl. Phys. Lett.* **70**, 2787 (1997).
8. Z. L. Liao, V. Diadiuk, J. N. Walpole, and D. E. Mull, *Appl. Phys. Lett.* **55**, 97 (1989).
9. Z. L. Liao, D. E. Mull, C. L. Dennis, R. C. Williamson, and R. G. Waarts, *Appl. Phys. Lett.* **64**, 1484 (1994).
10. J. S. Swenson, Jr., R. A. Fields, and M. H. Abraham, *Appl. Phys. Lett.* **66**, 1304 (1995).
11. T. A. Ballen and J. R. Leger, *Appl. Opt.* **38**, 2979 (1999).
12. W. W. Mullins, *J. Appl. Phys.* **30**, 77 (1959).
13. H. Nagai, Y. Noguchi, and T. Matsuoka, *J. Cryst. Growth* **71**, 225 (1985).
14. Z. L. Liao and H. J. Zeiger, *J. Appl. Phys.* **67**, 2434 (1990).
15. Z. L. Liao, *Mater. Chem. Phys.* **46**, 265 (1996).
16. Solid State Research Report, Lincoln Laboratory, MIT, 1991:3, p. 6.
17. See, for example, J. D. Jackson, *Classical Electrodynamics*, 3rd ed. (Wiley, New York, 1999), p. 118.

3. SUBMICROMETER TECHNOLOGY

3.1 MICROSCOPY AT WAVELENGTHS BELOW 200 nm

Ultraviolet microscopy is not a new idea. From the early part of the last century until the invention of the scanning electron microscope, reducing the wavelength λ into the near ultraviolet was one of the primary means of improving microscope resolution [1]–[3] $r = 0.61 \lambda/\text{NA}$. However, as the wavelength is decreased further, particularly below 200 nm, a second advantage of ultraviolet microscopy, increased contrast, becomes apparent. Many materials of interest have absorption edges in this region leading to large differences in optical properties among materials and thus to increased contrast. This article describes a reflected light microscope operating at 193 nm which is capable of imaging 1-nm-thick organic films on both reflective and transmissive substrates as well as 3-nm layers of thermally deposited SiO on Si.

The base platform is a Leitz SM-Lux microscope which has been extensively modified to operate with 193-nm light. A bright, compact cw source of 193-nm illumination is provided by a prototype rf microdischarge lamp developed at Rutgers, which is shown in the inset of Figure 3-1. A 22-kV ac voltage at 6 MHz is applied to two electrodes in an Ar and F₂ containing atmosphere. Electrical discharge creates an ArF plasma in the $\sim 100\text{-}\mu\text{m}$ space between the electrode tips, radiating up to 30 mW of 193-nm light into 4π . While dc microdischarge lamps have been used to produce deep ultraviolet (DUV) light [4]–[6] their electrodes quickly corrode in F containing atmospheres due to F⁻ ions formed in the discharge region [6]. Corrosion is reduced with a rf discharge as the period of the electrical signal is much shorter than the drift time of F⁻ ions between the electrodes, reducing the F⁻ flux at the electrodes and leading to electrode lifetime on the order of weeks with moderate use. The emission wavelength of this discharge lamp can be changed to any of a number of excimer wavelengths (157, 172, 248, 308 nm, etc.) simply by operating with a different gas mixture.

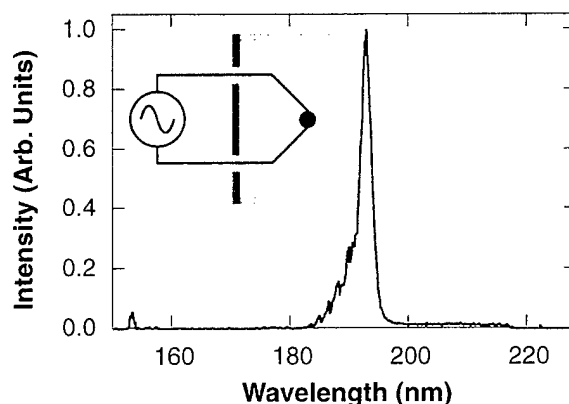


Figure 3-1. Spectrum of rf microdischarge lamp operating in an ArF atmosphere. Inset: schematic of the device showing small ($\sim 100 \mu\text{m}$) region of excited gas between two electrodes.

The light from this lamp is captured and focused with two ultraviolet-grade fused silica lenses. A dielectric mirror separates the 193-nm radiation from the faint blue component produced by the lamp and sends the light into the microscope. Inside the microscope, a dielectric beam splitter directs the light to the rear of the objective. After passing through the objective and illuminating the sample, the reflected light passes once more through the beam splitter before being imaged by a DUV-sensitive charge-coupled device (CCD) camera (Hamamatsu), only recently available commercially. Unfortunately, because of the small size of the source region ($<100\text{ }\mu\text{m}$ diameter), it must be greatly magnified to fill the field of the microscope. This accentuates small brightness variations in the source and makes uniform illumination difficult. The resulting variations in illumination across the field of view prevent us from making quantitative analyses of images obtained from the microscope. Although the microscope is optimized for 193-nm light, a simple white light illuminator can be placed behind the dielectric mirror, allowing imaging of the same sample under both visible and DUV illumination.

Because glass microscope objectives, even those designed for work in the near ultraviolet, are opaque at 193 nm, we use a set of Schwarzschild-type mirror objectives (15 \times , 0.25NA; 36 \times , 0.5NA). Beyond transparency in the DUV, a principal advantage of mirror objectives is their completely achromatic nature which allows the direct comparison of visible and DUV images without refocusing. However, the central obscuration of these lenses makes uniform illumination even more difficult while their relatively large aberrations limit the imaging, preventing us from taking full advantage of the increased resolution that should be available at this short wavelength. Refractive objectives made of fused silica and CaF_2 are available and we plan to upgrade this microscope in the near future.

The images in Figure 3-2 illustrate the contrast of 193-nm imaging with two types of samples. The first consists of thin layers of poly(hydroxystyrene) (pHOST), an organic polymer that is the base for many commercial DUV photoresists and is also a model compound for organic contamination of DUV optical systems. pHOST was spun cast to thicknesses from 1 to 10 nm on reflective Si and transparent quartz substrates. The films were then patterned by laser ablation through a Cr-on-quartz contact photomask. Figures 3-2(a) and 3-2(b) are images of the light reflected from the same area of a 5-nm film of pHOST on Si under 193-nm and white light illumination, respectively. Under 193-nm illumination, the pHOST film is clearly evident as a dark pattern on the bright Si background while in white light it is undetectable. The minimum thickness of pHOST that can be imaged on a Si substrate is limited by our ability to deposit thin films rather than the contrast of the imaging system. Likewise, Figure 3-2(c) shows a 1-nm film of pHOST on a quartz substrate. Note that in this case, the pHOST is more reflective than the quartz and is thus seen as light areas on a dark background. We have examined these thin organic films under a commercial visible light microscope in bright- and dark-field reflected light, phase contrast, and polarized light configurations as well as under a scanning electron microscope and have been unable to detect pHOST films much thinner than 10 nm. A second class of sample consists of a layer of SiO_2 thermally grown on Si wafers and patterned with photolithography followed by a wet HF etch. Figure 3-2(d) is a 193-nm image of a 3-nm-thick layer of oxide on Si.

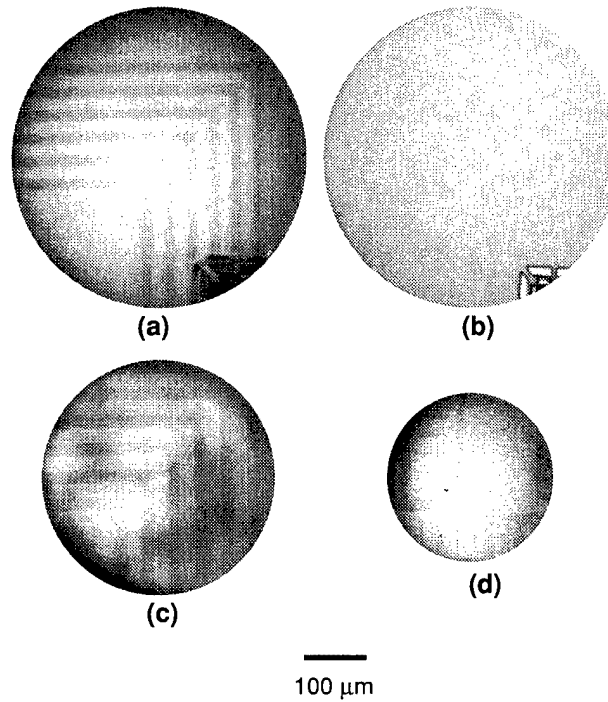


Figure 3-2. Images of thin films taken at 193 nm and in white light: (a) 5-nm layer of poly(hydroxystyrene) (pHOST) on a Si substrate taken at 193 nm; the pHOST is the darker region. (b) Image of the same field as in (a) taken in white light; the pHOST is undetectable. Note the Cr alignment feature at the bottom right of each image. (c) 1-nm layer of pHOST on a transparent quartz substrate. The difficulty of obtaining uniform illumination is apparent in this image. (d) 3-nm layer of thermally grown SiO_x on Si. The theoretical contrast of this image is only $\sim 4\%$ (see Figure 3-3).

In general, the reflectivity of a thin film on a reflective substrate is determined by the real and imaginary parts of its index of refraction, n and k . We have simulated the reflectivity contrast $\chi = 1 - R_1/R_2$ where R_1 and R_2 are the low and high reflectivity, respectively, for several materials commonly found in semiconductor processing. In the films studied here, the thickness $d \ll \lambda$ and interference effects are secondary. For strongly absorbing films on reflective substrates, the dominant contribution to χ is the absorption itself. Since many materials that are transparent in the visible and even the near ultraviolet absorb strongly in the DUV, microscopy at sub-200-nm wavelengths can dramatically increase contrast. As seen in Figure 3-3(a), the calculated χ of a 1-nm pHOST film at 193 nm is roughly $50\times$ greater than that for visible light at 500 nm and about $10\times$ better than near ultraviolet light at 315 nm. Similarly, Figure 3-3(b) shows that for a 1-nm film of Si_3N_4 , 193-nm light provides contrast that is $4\times$ better than 315 nm and $125\times$ better than 500 nm. Reflection contrast is much weaker for transparent films but even here DUV imaging provides a significant advantage. Figure 3-3(c) shows the reflection contrast for SiO_x on Si which is $5\times$ better in the DUV than the near ultraviolet and $25\times$ better than in the visible for a 3-nm layer, the thickness

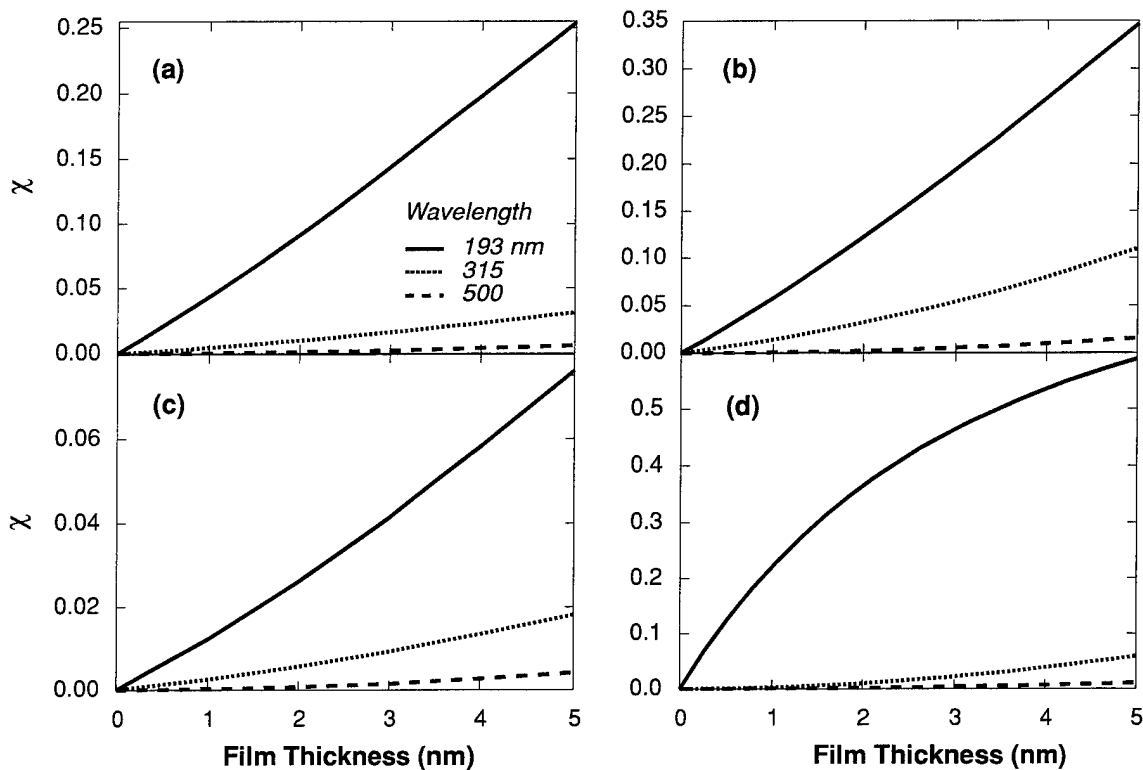


Figure 3-3. Calculated reflection contrast, where R_1 and R_2 are the low and high reflectivity, respectively, for (a) pHOST on Si, (b) Si_3N_4 on Si, (c) SiO_x on Si, and (d) pHOST on quartz. Note the clear advantage of deep ultraviolet illumination over near ultraviolet and visible in each case.

shown in Figure 3-2(d). Finally, for films on transparent substrates, contrast arises primarily from the index difference between the materials. Figure 3-3(d) shows the reflection contrast of pHOST on quartz where, for a 1-nm layer like that shown in Figure 3-2(c), 193-nm illumination is 65 \times better than 315 nm and 430 \times better than 500 nm.

The increased contrast available with sub-200-nm microscopy suggests many applications. The most immediate is the semiconductor lithography where the ability to resolve thin films is essential for inspection of substrates as well as optical components. Of particular interest is inspection at the wavelength used for exposure which can, given sufficient resolution, detect any contamination that interferes with patterning. In addition, since it is possible to change the wavelength of operation simply by changing the gas supplied to the lamp, it should be possible to determine the nature of the contaminants by comparing the image formed at several different wavelengths. In addition, the high absorbance of many materials in the DUV makes it possible to image the top layer of a multilayer semiconductor structure while avoiding interference from layers below [3]. We also hope to extend the domain of this microscope

beyond semiconductor processing. With all refractive optics, it should be possible to image features as small as 200 nm, and the other benefits of DUV imaging leave us hopeful for applications in forensics and biological imaging.

M. Switkes
M. Rothschild
M. Salvermoser*

3.2 STUDIES OF LASER-INDUCED CONTAMINATION AND CLEANING

As the semiconductor industry has transitioned to shorter wavelength exposure sources to pattern integrated circuits at higher resolutions, the demands on the cleanliness of the purge gas within the projection optics of the lithographic steppers have become significantly more demanding. Contaminants within the nitrogen purge gas even in the sub-ppm level can build up on surfaces through laser-stimulated deposition processes. Owing to the high number of surfaces and high absorptivity of laser deposits, particularly hydrocarbon based residues, we estimate one to two monolayers of hydrocarbon deposit on each surface would render a lithographic stepper operating at 157 nm useless because of transmission losses approaching 50%. With this in mind, under a Cooperative Research and Development Agreement with SEMATECH, we are performing systematic studies on the deposition and removal rates of various classes of contaminants to assist the stepper manufacturers in deciding the best route to prevent contamination from occurring. Options include active measures such as adding a reactive gas to the purge to ensure the removal rate exceeds the deposition rate, passive measures such as ensuring a contaminant is below a critical level such that over the lifetime of the tool, the total deposition is negligible, or preventive measures such as inserting a reactive gas in the purge stream periodically, for instance during maintenance schedules, to clean optical elements in situ.

To study the role of contaminants on transmission degradation, we have constructed a dedicated test bed which enables trace levels of contaminants to be injected into the purge gas and any resulting transmission changes monitored. Both lifetime and accelerated testing can be performed. The system has also been designed to allow the primary system variables expected within a lithographic stepper to be varied over typical operating conditions. Figure 3-4 shows schematically the optical test bed and gas delivery system. The basic test bed is similar to the test chamber used for bulk materials and optical coating evaluation. However, in one of the sample stations, a stainless steel vapor cell that accepts two 1-in.-diam windows can be inserted into the laser beam path. A gas mixing manifold has been constructed to inject trace levels of impurities between 10 ppb and ~1 ppm in the nitrogen purge stream flowing through the vapor cell. Residence times of the gas within the cell can be also be adjusted to investigate the effect of

*Author not at Lincoln Laboratory.

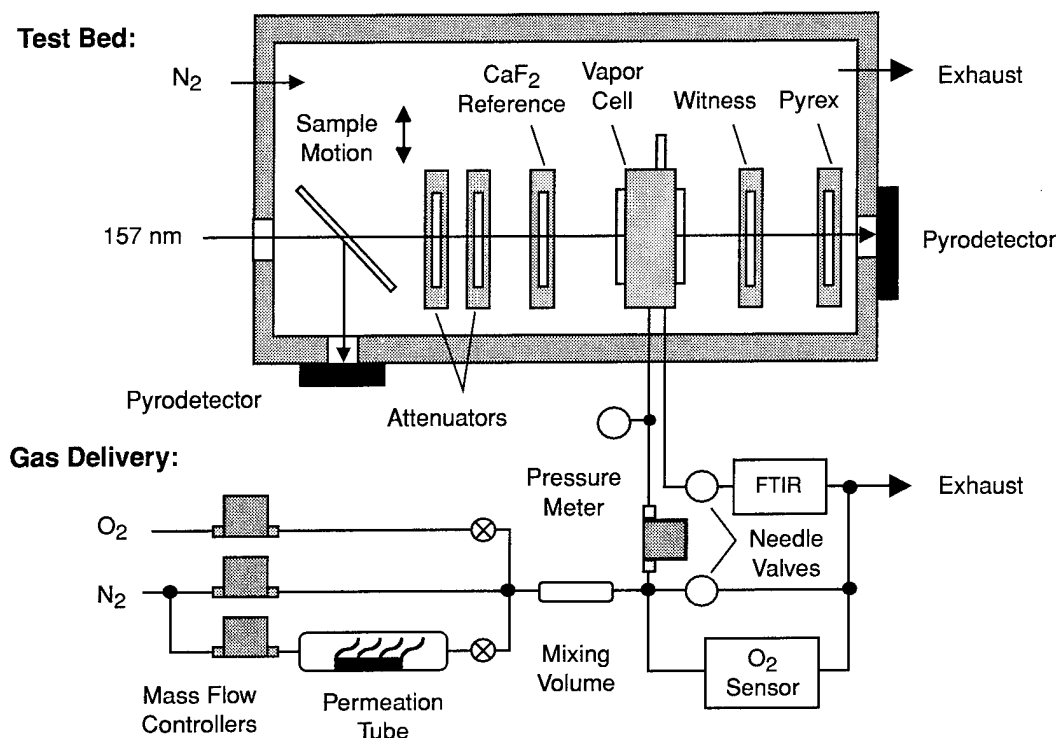


Figure 3-4. Schematic drawing of the contamination exposure system. Contaminants are introduced into the purge stream flowing through the vapor cell using calibrated permeation membrane devices. Four separate flow controllers are used to independently control dilution, oxygen level, and contaminant residence times within the vapor cell. With this arrangement, contamination levels can be conveniently controlled between 100 ppb and 10 ppm and oxygen levels between 0 and 50 ppm. A Fourier transform infrared (FTIR) based gas phase analysis system monitors the exhaust from the vapor cell to confirm contamination levels. Pressures within the vapor cell are held slightly above atmosphere to prevent any potential contaminants within the optical test bed from leaking into the vapor cell.

purge gas flow rate on contamination rates. In addition to mounting the vapor cell in one sample station, a CaF_2 reference piece is loaded in an alternate sample station to monitor any run-to-run variations. In addition, it is used to confirm that the purified nitrogen gas used to purge the test chamber does not contaminate the outside faces of the vapor cell windows. Rather, any drop in transmission measured through the vapor cell is due solely to surface losses from laser deposits on the inside faces. Furthermore, when evaluating contamination rates on coated optics, a coated sample is used as a witness sample. The witness sample is used to monitor any possible drops in transmission due to degradation of the coating rather than from contamination. Laser-based ratiometry is used to measure the change in transmission of the CaF_2 reference, witness sample, and vapor cell during irradiation. Transmission changes through the vapor cell represent the contamination rate on the two window faces facing the interior of the cell.

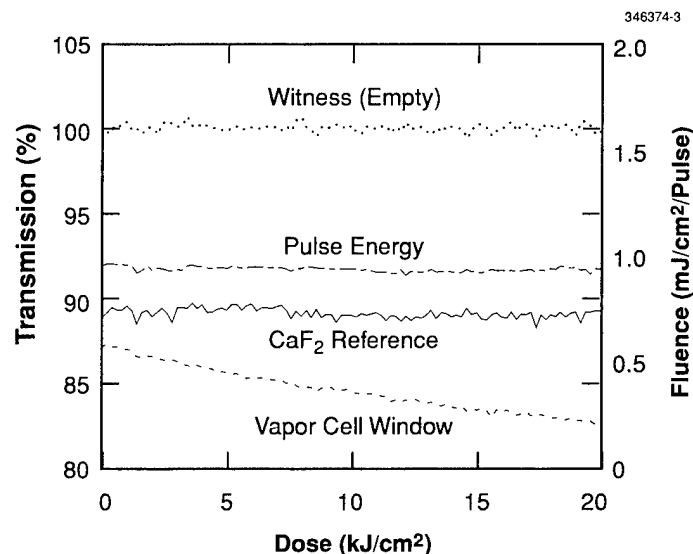


Figure 3-5. Transmission data collected with the contamination exposure system. In this experiment, 400 ppb of toluene was introduced into the purge gas flowing in the vapor cell. For clarity, this and subsequent graphs show the resulting transmission change over one CaF_2 window of the vapor cell.

Figure 3-5 shows a typical collection of transmission data taken with the contamination exposure system. It also dramatizes the high degree of sensitivity of optical transmission at 157 nm to gas phase contaminants even at the ppm level of contaminant. In this case, 400 ppb of toluene caused a transmission drop of 3-4% over a total exposure dose of 10 kJ/cm^2 . To put this in perspective, if this drop occurred on each surface of the stepper optics, within an hour under normal operating conditions, the lens would be effectively opaque to 157-nm irradiation.

During the period of contamination, there are two competing mechanisms occurring: the deposition of material and back reaction from cleaning. For the case of hydrocarbon-based impurities, it is well established that oxygen can be used to enhance the cleaning rates [7],[8]. One possible technique to prevent contamination is to purposely bleed trace levels of oxygen to compete with the deposition process. The primary constraint is that the total level of oxygen must not significantly attenuate the exposure source through the projection optics, which at 157 nm will probably limit oxygen to levels below 10 ppm. Shown in Figure 3-6 are transmission traces taken as the oxygen concentration is increased from 0.4 to 13 ppm in 3 ppm of toluene. There are a number of interesting features on these curves. Clearly, the introduction of oxygen has slowed the contamination rate. In addition, there is initially a rapid drop in transmission during the initial phases of irradiation even at higher oxygen levels. From the absorption value of hydrocarbon-based residues, we estimate this contamination rate drops off after approximately 1 monolayer is deposited. This implies either the cleaning or deposition rate is varying as the film builds up. We are

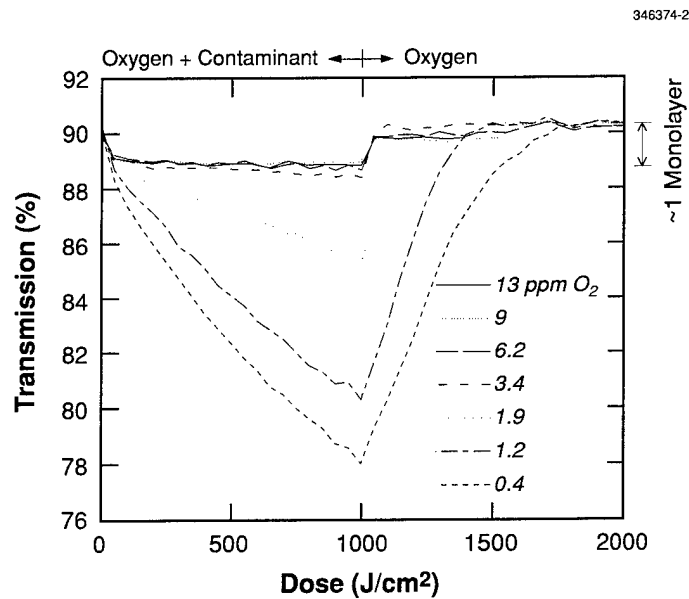


Figure 3-6. Transmission change as the oxygen level is varied between 0.4 and 13 ppm in 3 ppm of toluene. After the first $1000 \text{ J}/\text{cm}^2$, the contaminant arm of the gas delivery manifold is turned off and full transmission was restored.

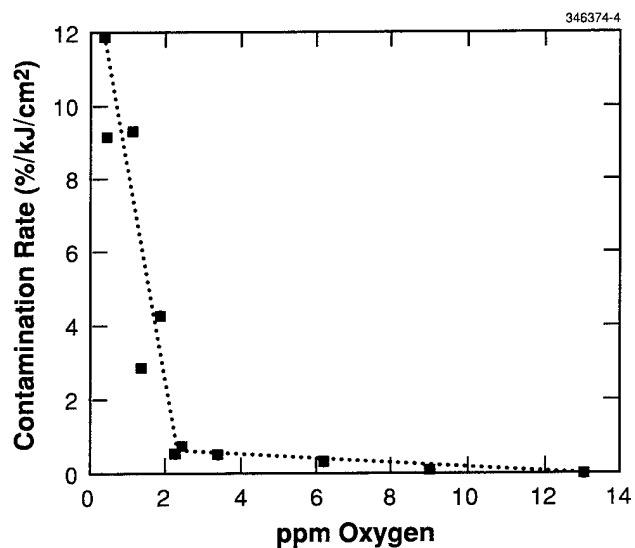


Figure 3-7. Estimated contamination rate based on the transmission data taken in Figure 3-6 after first monolayer is deposited.

investigating this further, but the data indicate both are changing. During the cleaning stage (doses 1000–2000 kJ/cm²), the cleaning rate appears to slow down over the final monolayer. Shown in Figure 3-7 are the calculated contamination rates taken from the slopes of the transmission curves after approximately 1 monolayer of deposit. It again highlights a nonlinear threshold type of behavior. In this experiment, the contamination stops when the ratio of oxygen to toluene exceeds 4:1. In general, we expect that the required ratio of oxygen to toluene will be a function of the absolute value of toluene present. From the contamination and cleaning rates, the actual deposition rate can also be predicted. Shown in Table 3-1 is the estimated rate data taken from the slopes of the transmission curves after the first monolayer is deposited. The deposition rate is ~12.4% per kJ/cm² per ppm toluene. Again, this emphasizes that either the deposition rate for a chemical species has to be zero, or some form of cleaning is required. For instance, if no cleaning mechanism were present, even at 1-ppt level of toluene, within approximately 1 week, the optics within a lithographic stepper operating at 157 nm would be effectively opaque.

TABLE 3-1
Calculated Deposition Rates at 3 ppm of Toluene

O ₂ (ppm)	Contamination Rate (%/kJ/cm ²)	Cleaning Rate (%/kJ/cm ²)	Deposition Rate (%/kJ/cm ²)
0.4	11.9	24.5	36.4
1.2	9.3	29.8	39.1
1.9	4.3	32.0	36.3

Our initial results indicate oxygen can be used to limit the effects of hydrocarbon-based contaminants. We are currently in the process of exploring the effects of additional representative hydrocarbon contaminants as well as other non-hydrocarbon materials including fluorocarbons and organosilicons. In addition, studies are under way to determine whether the rates of contamination differ on coated samples and whether changes are permanent, or can be subsequently cleaned in situ.

T. M. Bloomstein V. Liberman
S. T. Palmacci M. Rothschild

REFERENCES

1. M. Born and E. Wolf, *Principles of Optics*, 3rd ed. (Pergamon, London, 1965).
2. J. R. Wood and D. A. I. Goring, *J. Microsc.-Oxford* **100**, 105 (1974).
3. P. A. Heimann and R. Urstadt, *Appl. Opt.* **29**, 495 (1990).
4. A. El-Habachi and K. H. Schoenbach, *Appl. Phys. Lett.* **73**, 885 (1998).
5. A. El-Habachi and K. H. Schoenbach, *Appl. Phys. Lett.* **72**, 22 (1998).
6. M. Salvermoser, D. E. Murnick, J. Wieser, and A. Ulrich, *J. Appl. Phys.* **88**, 453 (2000).
7. B. G. Ranby and J. F. Rabek, *Photodegradation, Photo-oxidation and Photostabilization of Polymers* (Wiley, New York, 1975), Chap. 5.
8. T. M. Bloomstein, M. Rothschild, V. Liberman, D. E. Hardy, N. N. Efremow, Jr., and S. T. Palmacci, *Proc. SPIE* **4000**, 1537 (2000).

4. BIOSENSOR AND MOLECULAR TECHNOLOGIES

4.1 RESPONSE OF B CELLS TO SUPERPARAMAGNETIC PARTICLE SIMULANTS

Increasing awareness of the threat posed by biological weapons underscores the need for devices capable of sensitive, rapid, and reliable detection and identification of bioagent releases. To meet this need, we have been developing a novel bioelectronic sensor for the detection of viral and bacterial pathogens that exploits engineered elements of the natural immune response as described previously [1]–[3]. The cornerstone of the CANARY (Cellular Analysis and Notification of Antigen Risks and Yields) sensor is a cell line derived from B cells, a type of white blood cell that expresses antibodies on the outer membrane that bind specifically to a particular molecule (antigen). Antibody-antigen interaction generates a signal inside the B cell which undergoes several levels of amplification and causes an increase in the internal calcium-ion concentration. We have engineered (i.e., added genomic material to) an immortal B cell line (atypical B cells that can be cultured outside a living host and replicate by cell division) to express the photoprotein aequorin. This protein, which is normally found in luminescent jellyfish, produces light in response to increases in calcium concentration by oxidizing its cofactor, coelenterazine. The aequorin produced inside the engineered B cell emits light as calcium levels rise following antigen binding. In this way, we have developed cells that emit photons following exposure to specific bioagents.

While the production of B cell lines engineered to respond to bacterial agents is nearing completion, we have produced appropriate simulants for bacteria to assist the development of a fieldable CANARY sensor. Previous demonstrations of specific photodetection of bioagent simulants used an image-intensified charge-coupled device camera to image the antigen-specific response of B cells in prototype microfluidic packages to protein-based simulants that displayed multiple copies of phosphoryl choline (PC). Because the mixing and settling behavior of relatively large bacterial particles (typically 1–3 μm in diameter) in suspension differs significantly from that of soluble proteins (typically 3–10 nm in diameter) in solution, we chemically linked PC to 2.8- μm -diam streptavidin (SA) coated superparamagnetic beads (SA-beads) in an attempt to produce a more realistic simulant for bacterial challenges to our sensor. We now report the characteristics of these PC/SA-beads as simulants for large-particle stimulation of photon emission from B cells and the results of initial experiments using the PC/SA-beads to determine the sensitivity and response time of the CANARY sensor.

A typical experimental setup as depicted in Figure 4-1 consists of a perfusion channel mounted on an image-intensified charge-coupled device camera housed in a dark enclosure for observation. The perfusion chamber was prepared by introducing a sufficient number of B cells to cover the thin glass that makes up its bottom surface. The B cells quickly settle and attach to the glass surface forming a monolayer. Liquid samples containing test substances are flowed into the perfusion chamber with a remotely operated pump. Settling or diffusion brings these substances into contact with the B cells causing them to emit light, a portion of which is collected by the camera.

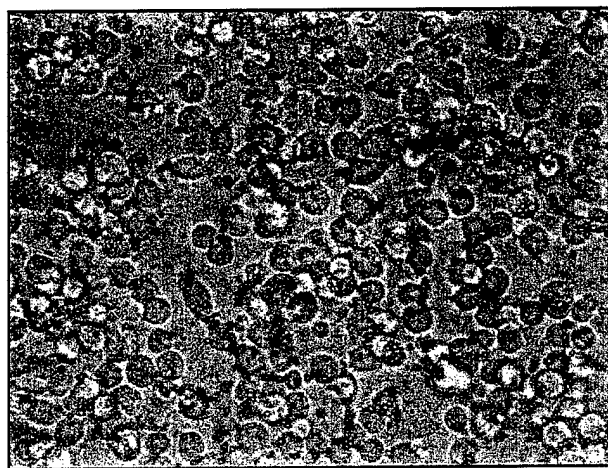
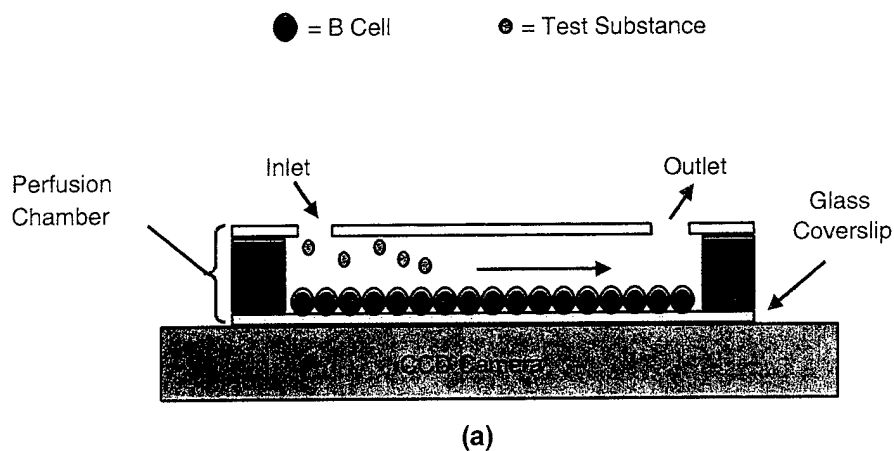


Figure 4-1. Typical perfusion chamber experimental setup: (a) Schematic of chamber setup. (b) Photomicrograph of B cells (large spheres) and 2.8- μm -diam phosphoryl choline (PC)/SA-beads (small spheres) mixed at a ratio of 4 beads/cell.

The sensitivity of detection of PC/SA-bead simulants was tested by observing changes in the photon emission intensity produced by serial dilutions of the PC/SA-beads. Only the trials containing functionalized PC/SA-beads demonstrated increased light output compared to the background levels of light produced by either cells alone or cells mixed with unfunctionalized SA-beads. As shown in Figure 4-2, the magnitude of the photon output decreases and the peak response time increases as the approximate number of PC/SA-beads is reduced from 40 beads/cell to 0.4 beads/cell. At 0.04 beads/cell the signal was

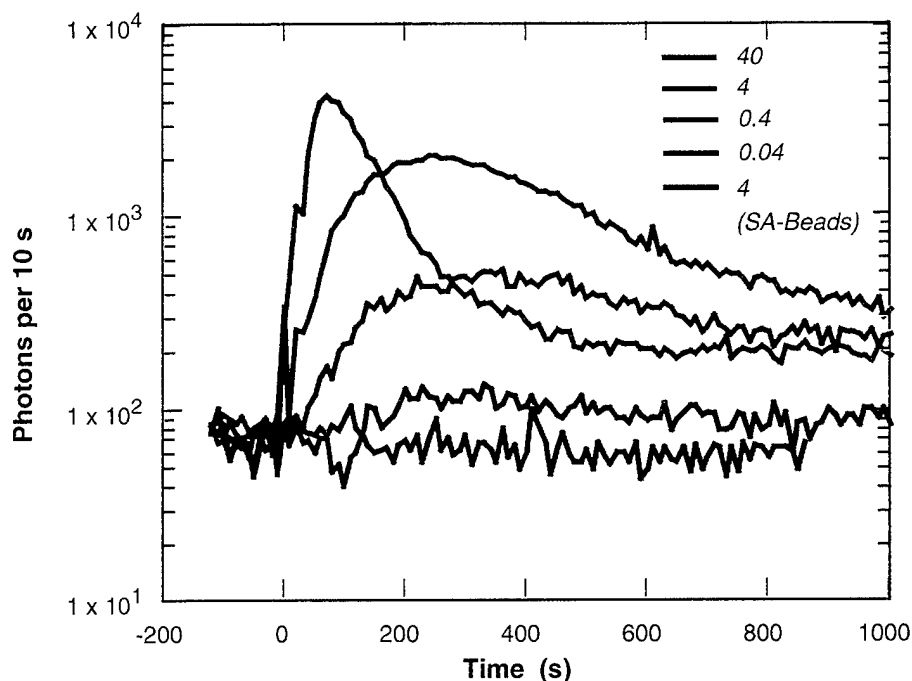


Figure 4-2. Dose-response behavior of stimulation of adhered B cells with PC/SA-beads. The numbers used to label each curve represent the average number of beads/cell in each individual experiment plotted.

just distinguishable from background noise in this format. The time required to yield ~90% of the maximum photon output ranged from ~1 min at 40 beads/cell to ~4 min at 0.8 beads/cell. In terms of absolute numbers of particles detected, this format allowed detection of as few as 10^4 particles in $50\ \mu\text{l}$ in the case of 0.04 beads/cell. Since only a portion of the channel was integrated to produce the data displayed in Figure 4-2, it may be possible to detect significantly fewer particles at similar concentrations by simply reducing the total volume of the reaction.

Because the simulants we are using are superparamagnetic beads we were able to use magnetic fields to localize a limited number of beads within a small region of the perfusion channel. We have used two variations of this approach to investigate the absolute particle number sensitivity of the CANARY sensor. In the first implementation, a limited number of beads were delivered into the perfusion chamber and isolated in a localized area on the top surface by a small magnet while B cells were added underneath and allowed to form a monolayer under the beads. The photon output of the cell layer was monitored after removal of the magnet as the beads fell under the influence of gravity and came into contact with the cells below. As the example in Figure 4-3 shows, we are able to distinguish from background the photon output

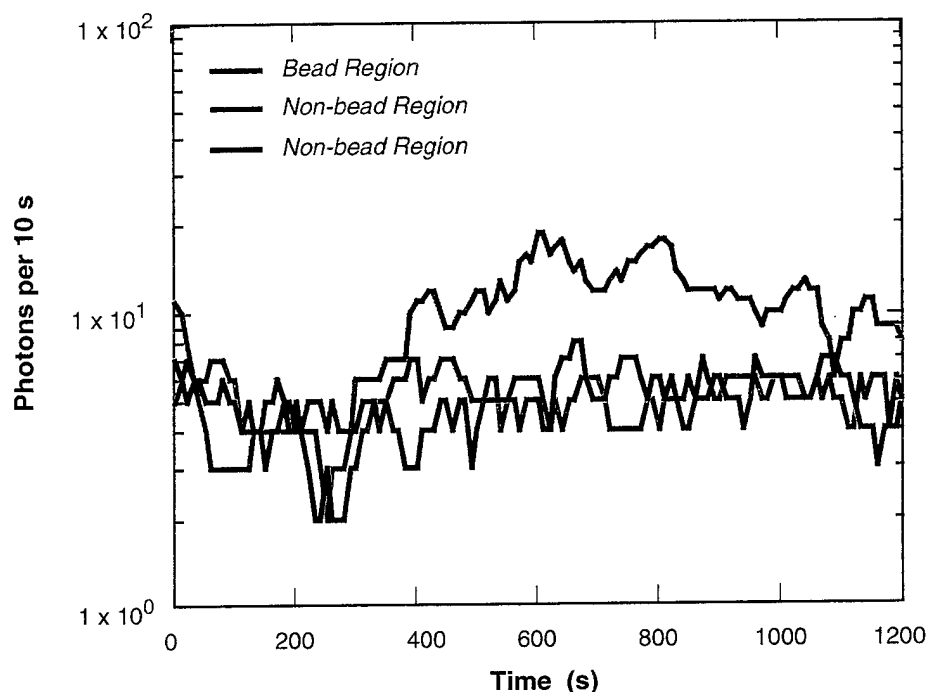


Figure 4-3. Increased photon output after release of approximately 1000 localized PC/SA-beads.

stimulated by as few as 1000 bead-simulants using this format with maximum photon output occurring ~8 min after bead release. For comparison, standard immunoassays require ~15 min to produce maximum signal and have a limit of detection of $\sim 10^5$ antigens.

The observation that the response time in the passive format was limited by the time required for the beads to fall into contact with the cells motivated preliminary attempts to actively concentrate PC/SA-beads onto a cell layer from a dilute solution using a magnetic field. A monolayer of B cells was attached to the upper surface of a perfusion channel placed on the camera. A magnet placed above the cells was used to attract beads from a dilute suspension to the upper cell layer as the beads were pumped through the chamber while monitoring photon emission from below. Figure 4-4 shows results from an initial experiment using this active capture strategy that demonstrate successful detection of the captured portion of the approximately 3000 total beads delivered past the magnet in 150 μ l of solution. Based on our prior experience, ongoing optimization of the delivery parameters including magnetic field orientation and flow rate should provide detection limits for this active capture mode that are equal to, if not better than, the 1000 particles reliably detected in the passive bead drop format. The peak photon emission occurs in <2 min at this dilution compared to the 8 min required to reach peak photon output with passive presentation of a similar number of beads.

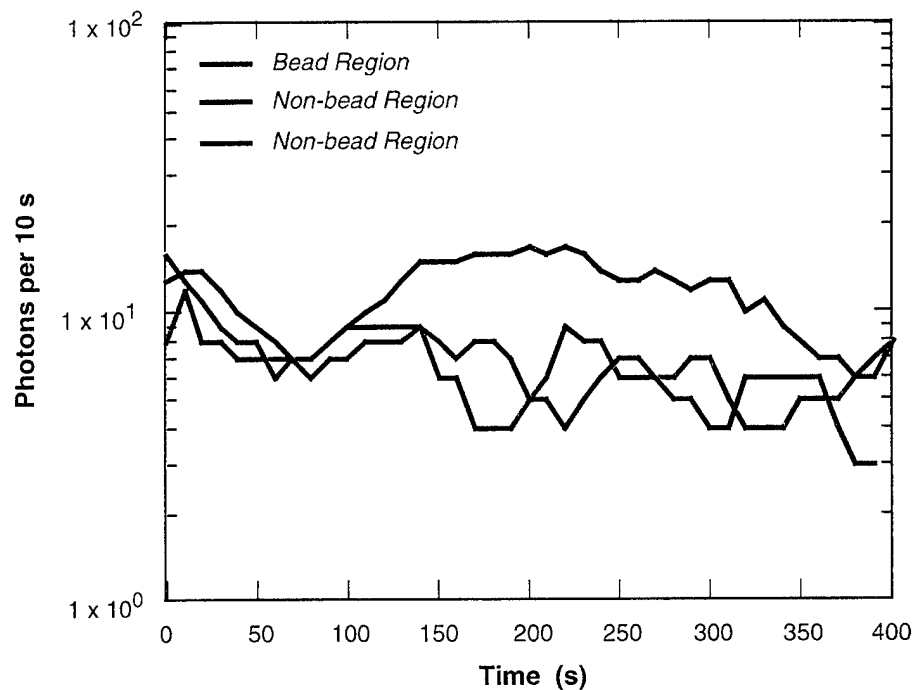


Figure 4-4. Increased photon output after active magnetic capture of ≤ 3000 beads delivered in 150- μ l volume.

Although the actual agents are not magnetizable, they could be captured using magnetic particles or subjected to other forces (centrifugal, electrophoretic, etc.) to produce a similar acceleration of the response of the CANARY sensor to very dilute samples of micron-scale particles including bacteria. Current efforts are being focused on development and evaluation of active antigen presentation strategies that are compatible with the range of operational implementations envisioned for a field-deployed CANARY sensor.

J. D. Harper	R. H. Mathews
F. E. Nargi	M. S. Petrovick
T. H. Rider	A. M. Young
M. A. Hollis	J. Chen

REFERENCES

1. Solid State Research Report, Lincoln Laboratory, MIT, 1998:4, p. 27.
2. Solid State Research Report, Lincoln Laboratory, MIT, 1999:1, p. 21.
3. Solid State Research Report, Lincoln Laboratory, MIT, 1999:2, p. 21.

5. ADVANCED IMAGING TECHNOLOGY

5.1 A 32×32 LASER RADAR IMAGER BASED ON A GEIGER-MODE AVALANCHE PHOTODIODE ARRAY INTEGRATED WITH A CMOS DIGITAL TIMING CIRCUIT

Lincoln Laboratory has been developing imaging laser radar systems based on Geiger-mode avalanche photodiode (APD) arrays as a receiver imaging sensor technology. These systems function by transmitting a subnanosecond laser pulse to illuminate the scene of interest, and imaging the return onto the APD array. Each APD produces a fast (subnanosecond) electrical pulse when it detects a photon, and the time of occurrence of this pulse is measured and used to deduce the photon flight time to and from the corresponding point in the scene. Thus, the system produces an image whose pixel values represent ranges rather than reflected intensities. A laser radar system was built and demonstrated at the Laboratory that used a 4×4 array of silicon APDs, and a frequency-doubled passively Q -switched Nd:YAG microchip laser [1],[2] ($\lambda = 532$ nm) in the transmitter. The field of view of the 16-pixel array was raster scanned using scanning mirrors to produce 128×128 images. The pulses from the APD were amplified and sent to external rack-mounted timing modules. A variety of indoor and outdoor scenes were imaged, both at day and at night, and the three-dimensional images compared to conventional intensity images of the same scenes [3]–[7].

Despite the success of this demonstration, the system is fairly large owing to the need both for mechanical scanning and for external rack-mounted electronics. Furthermore, only 16 pixels of imagery are acquired on each laser pulse, severely limiting the frame rate of the system. The system is therefore being upgraded to incorporate a larger (32×32) focal plane array with integrated CMOS timing electronics. The focal plane array is a compact solid state device that produces digital timing values.

We have recently completed fabrication of the very first such 32×32 APD/CMOS imager. The 32×32 silicon APD array was fabricated on a 6-in. silicon wafer at Lincoln Laboratory's Microelectronics Laboratory. The fabrication process and characterization of these APDs was described previously [8],[9]. The detectors used have a $30\text{-}\mu\text{m}$ -diam circular active area and a $100\text{-}\mu\text{m}$ pixel-to-pixel spacing. The CMOS timing circuit was fabricated through the MOSIS foundry service using a $0.35\text{-}\mu\text{m}$ CMOS process.

The timing chip is a 32×32 array of timing circuits, each occupying a $100 \times 100\text{-}\mu\text{m}$ area. Figure 5-1 shows a photograph of a portion of the chip. Each circuit has a small ($20\text{ }\mu\text{m}$) bond pad where the connection to the corresponding APD is made. Figure 5-2 is a block diagram of the timing circuit. A high-speed clock is generated on the chip and broadcast to all the timing circuits. In each circuit the clock drives a 15-bit counter through a tri-state inverter. The photon detection pulse from the corresponding APD puts this tri-state inverter into its high-impedance state, simultaneously stopping the counter and storing the state of the clock. The 16 bits comprising the counter state and the clock state encode the photon arrival time with a resolution of half the clock period. A secondary clock is generated by delaying the high-speed

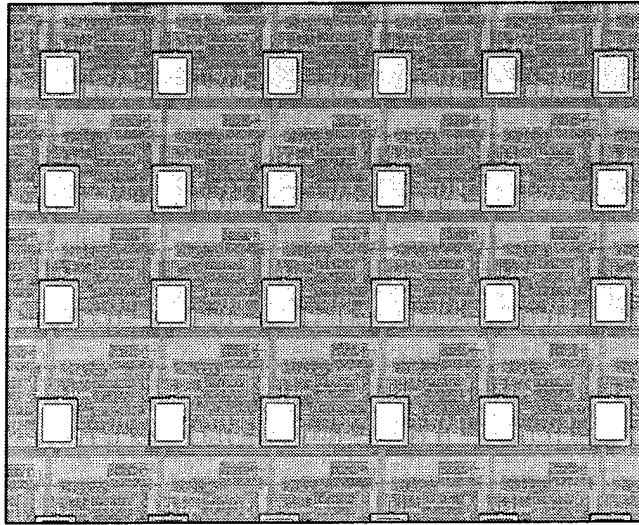


Figure 5-1. Photomicrograph of portion of 32×32 array of CMOS timing circuits.

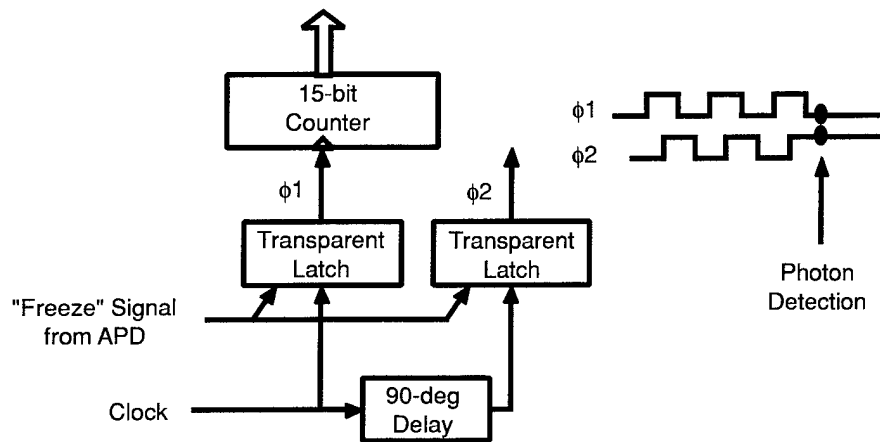


Figure 5-2. Block diagram of timing circuit, which consists of 15-bit pseudorandom counter, and clock phase detection circuitry to measure subperiod time intervals.

clock by 90° . The secondary clock is also broadcast to all the timing circuits and its state is stored by a tri-state inverter when photon detection occurs. The photon arrival time is thereby encoded with a resolution of one quarter of the clock period. The clock is generated by a 9-stage ring oscillator with its own separate power supply; the clock frequency can be adjusted by changing this power supply voltage. Timing circuit simulations indicate a nominal high-speed clock frequency of 500 MHz. A digital delay line whose delay is adjusted by a chip input voltage is used to generate the secondary clock. Bench tests of these CMOS chips confirm functionality up to clock rates of 400 MHz. The speed limitation is due to power supply droop due to resistive and inductive parasitics, both on chip and in the package. A chip with an improved power supply distribution and decoupling capacitors is in fabrication.

The CMOS chip was integrated with the APD array using a process known as bridge bonding, in which the CMOS chip is epoxied to the APD array, the APD wafer substrate removed to back illuminate, and vias etched between the APDs to make the electrical connections to the timing circuits. The process has been described previously [10]. Figure 5-3 is a photomicrograph of the completed 32×32 device.

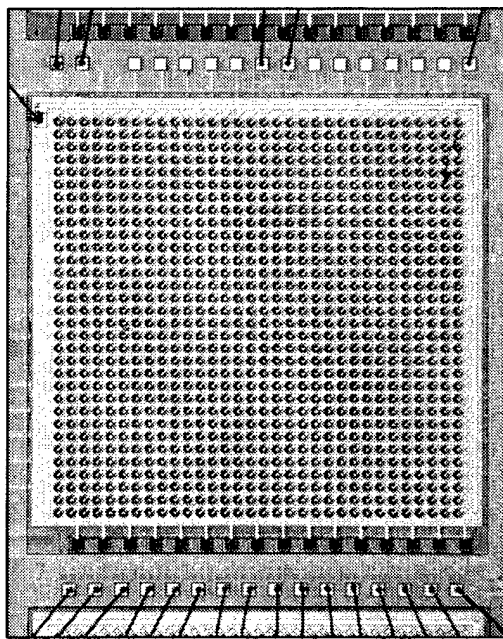


Figure 5-3. Photomicrograph of 32×32 bridge-bonded avalanche photodiode (APD)/CMOS laser radar imager.

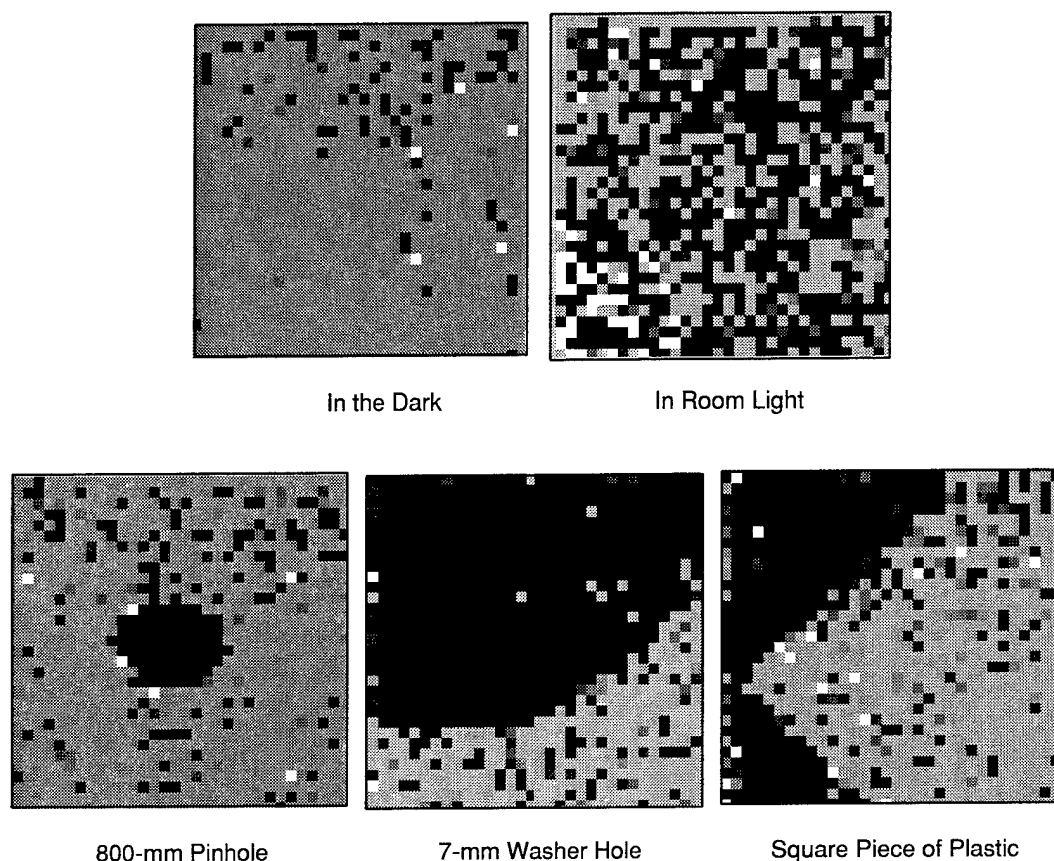


Figure 5-4. “Negative-tone” images obtained by illumination of the imager with patterns of steady light.

Initially, the device was tested using spatially varying patterns of steady light, either room light or coronal light from a flashlight, projected onto the device. Illuminated APDs detected a photon very early during the timing interval, and the corresponding pixels reported out very low detection-time values. APDs that were masked from the light, in most cases, did not fire at all during the timing interval and these pixels reported out timing values corresponding to the duration of the timing interval (250 ns). The timing values were displayed as grey scale (black corresponding to immediate detection, light grey corresponding to 250 ns), and therefore the displayed images are “negative-tone” replicas of the illumination patterns. Figure 5-4 shows the images obtained in the dark, in room light, and with coronal flashlight illumination through a pinhole, through a washer hole, and around the edges of a square piece of black plastic. The white pixels represent pixels reporting values in excess of 250 ns, which indicates that a bit error was made. This is believed to be a result of power supply bounce due to the above mentioned parasitics.

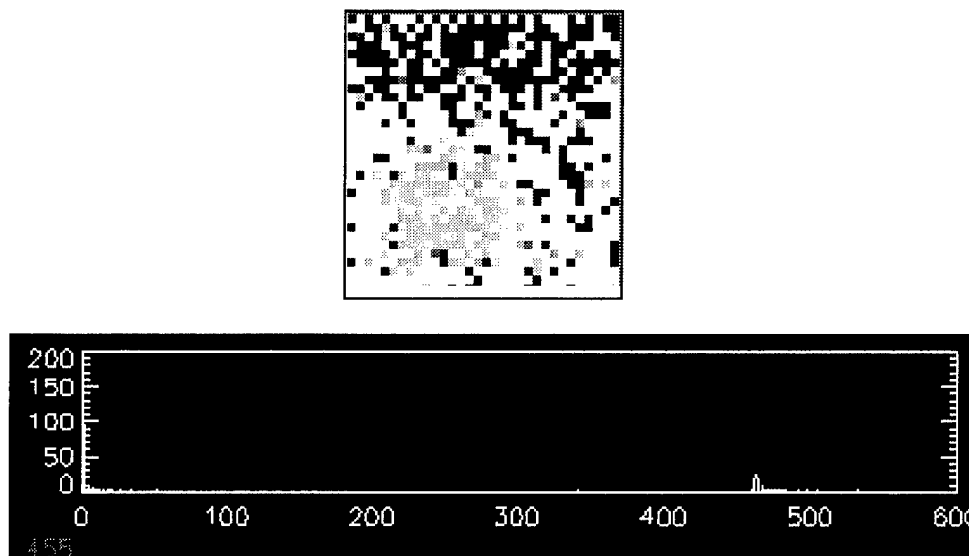


Figure 5-5. Image obtained by illumination of portion of imager with timed pulse of green light from light-emitting diode (top), and corresponding timing histogram (bottom).

In this experiment the p side of the APDs was biased at about -23.5 V, a few tenths of a volt in magnitude below the avalanche breakdown voltage, and the CMOS circuit turned the APDs on by charging the n side to $+4$ V. In order to confirm that the response of the APDs to the light was indeed Geiger-mode pulses, the magnitude of the p side bias on the APDs was decreased to more than a volt below the avalanche breakdown. This resulted in the disappearance of the black pixels, indicating that the images are not due to linear mode photocurrents.

In order to verify the timing functionality of the device, a fast green light-emitting diode (LED) ($\lambda = 562$ nm, pulse duration = 1.4 ns, pulse energy = 140 fJ), was used to illuminate a portion of the device. The pulse was timed to occur in the middle of a 2.5 - μ s timing interval. Figure 5-5 shows the resulting image, and a timing value histogram. The gray area corresponding to the LED illumination is clearly visible in the lower left corner of the image. The horizontal axis of the histogram is elapsed clock periods, and the clock period used was about 3 ns. The peak in the histogram corresponds to the arrival time of the LED pulse at the APD, but the spread in the timing values is not understood. There are also many dark pixels in the upper portion of the array, which may be due either to high dark count rates or leakage current. More thorough characterization is being pursued to understand these phenomena and to measure performance metrics such as detection probability and timing precision.

B. F. Aull
A. L. Loomis

REFERENCES

1. J. J. Zayhowski and C. Dill III, *Opt. Lett.* **19**, 1427 (1994).
2. J. J. Zayhowski, *Rev. Laser Eng.* **29**, 841 (1998).
3. D. G. Fouche, B. F. Aull, M. A. Albota, R. M. Heinrichs, J. J. Zayhowski, M. E. O'Brien, and R. M. Marino, presented at Military Sensing Symposium: Active Electro-Optic Systems, Wright-Patterson Air Force Base, Ohio, April 2000.
4. D. G. Fouche, M. A. Albota, B. B. Kosicki, R. K. Reich, B. E. Player, M. E. O'Brien, R. M. Heinrichs, B. F. Aull, J. J. Zayhowski, and R. M. Marino, presented at Military Sensing Symposium: Camouflage, Concealment and Deception, Charleston, S.C., March 2000.
5. R. M. Marino, R. M. Heinrichs, D. G. Fouche, M. A. Albota, B. F. Aull, S. Kaushik, and J. J. Zayhowski, presented at Military Sensing Symposium: Missile Defense—Sensors, Environments, and Algorithms, Charleston, S.C., January 2000.
6. D. G. Fouche, B. F. Aull, S. Kaushik, J. J. Zayhowski, R. M. Heinrichs, A. H. Loomis, M. A. Albota, and B. E. Player, presented at Infrared Information Symposium: Active Systems, Monterey, Calif., February 1999.
7. R. M. Heinrichs, B. F. Aull, S. Kaushik, D. G. Kocher, and M. A. Albota, presented at Infrared Information Symposium: Active Systems, Albuquerque, N.M., March 1998.
8. Solid State Research Report, Lincoln Laboratory, 1997:3, MIT, p. 31.
9. Solid State Research Report, Lincoln Laboratory, 1996:3, MIT, p. 39.
10. Solid State Research Report, Lincoln Laboratory, 1999:3, MIT, p. 33.

6. ANALOG DEVICE TECHNOLOGY

6.1 INTERMODULATION DISTORTION IN YBCO BICRYSTAL GRAIN BOUNDARIES

Grain boundaries and grain-boundary junctions in high-temperature-superconducting (HTS) thin films are of great interest because of their importance in both device applications and fundamental physics. This group has previously presented measurements of the microwave-frequency power dependence of engineered grain boundaries as a function of grain-boundary angle [1]. The conclusion of that work was that the low-angle grain boundaries were not the source of the nonlinear surface resistance in epitaxial thin films. Figure 6-1 summarizes the results. It shows the measured reciprocal of the unloaded Q_u of a stripline resonator, which is proportional to the resistance, vs rf current for several grain-boundary angles. The effective rf critical current for angles less than 5° was found to be indistinguishable from that of the rest of the film. Since high-quality epitaxial films do not contain grain boundaries greater than approximately 2° [2], one concludes that such low-angle grain boundaries are not causing the nonlinear surface impedance. The arguments are given in more detail in [1]. In this report, we present measurements of the intermodulation distortion (IMD) in the same range of grain-boundary angles. The results of the IMD measurements lead to a similar conclusion as the measurements of the nonlinear surface impedance. The low-angle grain boundaries are not the source of the IMD observed in epitaxial thin films.

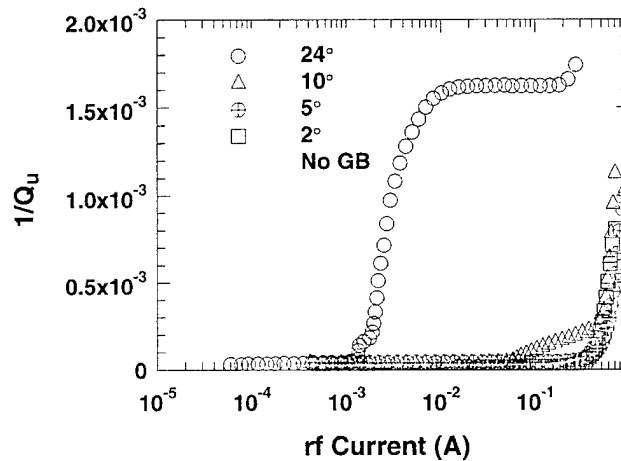


Figure 6-1. Plot of $1/Q_u$ as a function of rf current at $T = 50$ K. The curves are largely indistinguishable until the rf current reaches a level where the grain boundary (GB) causes the $1/Q_u$ to increase compared to the film on the single-crystal substrate. This increase is only seen in the 24° and 10° grain boundary.

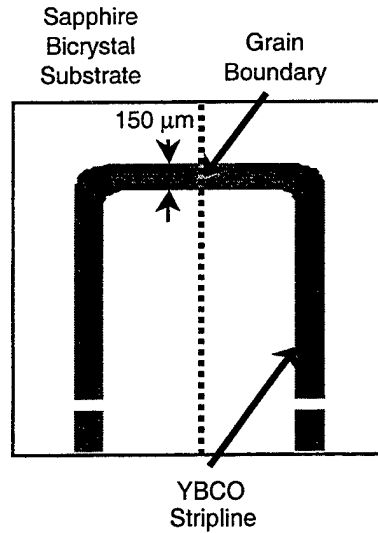


Figure 6-2. Schematic view of resonator used in the experiments. The engineered grain boundary is located at the midpoint of the patterned line.

The grain boundaries used in this study are the same ones that we have reported previously [1],[3]. They were fabricated at the National Institute of Science and Technology at Boulder [4] in 140-nm-thick, epitaxial, *c*-axis-oriented YBCO films deposited by laser ablation on 1×1 -cm, *r*-plane (1012), sapphire bicrystal substrates with misorientation angles of 2, 5, 7.5, 10, and 24° and single-crystal substrates. To characterize the microwave properties of the grain boundaries, we used a $\lambda/2$ microstrip-resonator configuration that allows us to distinguish the effects of the grain boundary from those of the rest of the film. The resonator, shown in Figure 6-2, is patterned such that the junction is positioned at the midpoint of the microstrip, spanning the entire width of $150 \mu\text{m}$ of the patterned line. The resonance frequency f_1 of the fundamental mode is 4.4 GHz with overtone resonant modes at $f_n \sim nf_1$ where n is an integer. At resonance, the fundamental mode is a half-wavelength standing wave with a current maximum at the midpoint of the resonator line, where the fabricated junction is positioned. In contrast, the $n = 2$ mode is a full wavelength with a current node at the position of the junction. Therefore, by comparing the measured results of these two modes, we can separate the impedance of the engineered grain boundary from that of the remainder of the superconducting film. This resonator technique has previously been used to measure the microwave power-handling properties of the grain boundaries [1],[5].

We have measured the IMD using the standard two-tone method, in which two tones f_A and f_B of equal amplitude are applied to the resonator. The tones are separated symmetrically about the center frequency of the resonator by an amount Δf such that both tones are within the 3-dB bandwidth of the resonator. We then measure the output power in the fundamental tones at f_A and f_B and the third-order mixing products $2f_A - f_B$ and $2f_B - f_A$ in a spectrum analyzer as a function of the input power.

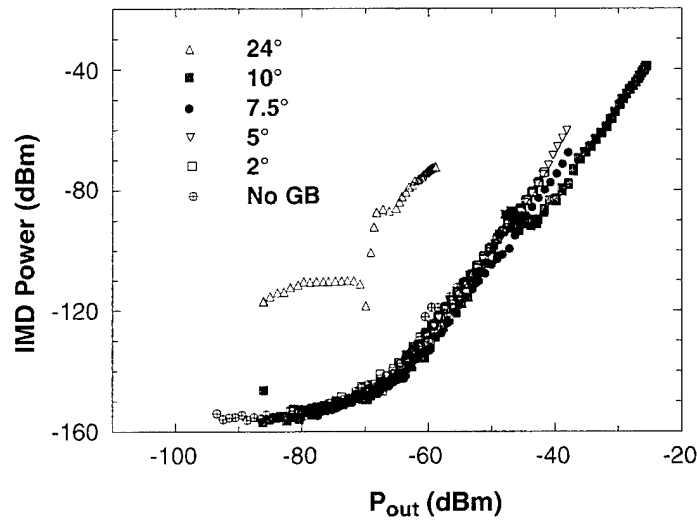


Figure 6-3. Results of measurement of third-order intermodulation distortion (IMD) power at 30 K for the various grain-boundary angles as shown. We plot IMD power vs output power at the fundamental, P_{out} . The 24° grain boundary shows a marked increase in IMD, but the other angles do not show any systematic variation. From this we conclude that the low-angle grain boundaries are not the source of IMD in epitaxial thin films.

Figure 6-3 is a plot of the third-order IMD power vs the power out at the fundamental mode, P_{out} , of 4.4 GHz at 30 K, with $\Delta f = 2$ kHz. The P_{out} is determined by the circulating current and insertion loss of the resonator. Thus, plotting the IMD vs P_{out} out normalizes the Q values and insertion losses of the different resonators. The measurements were done at several temperatures and these are representative results. As noted in the caption, the 24° grain boundary is the only one that shows a marked increase of the third-order signal. The others show variation but no systematic trends vs grain-boundary angle. These results lead to the conclusion that the third-order IMD arises from some other mechanism than the low-angle grain boundaries. As discussed in [1] this conclusion rests on the assertion that the epitaxial film contains only grain boundaries of substantially less than 2° . While Figure 6-3 shows the results for 30 K, similar results were found at other temperatures with the exception that the 10° grain boundary showed elevated IMD relative to the other values for temperatures above 75 K.

The results of the IMD measurements presented are consistent with the conclusion that the low-angle grain boundaries are not the source of the IMD in epitaxial films. This also agrees with our earlier finding that low-angle grain boundaries are not the source of the nonlinear surface impedance. It is generally believed that epitaxial films do not contain grain boundaries of greater than 2° .

D. E. Oates	H. Xin
G. Dresselhaus*	M. S. Dresselhaus*

*Author not at Lincoln Laboratory.

REFERENCES

1. Y. Habib, C. J. Lehner, D. E. Oates, L. R. Vale, R. H. Ono, G. Dresselhaus, and M. S. Dresselhaus, *Appl. Phys. Lett.* **73**, 2200 (1998).
2. A. F. Marshall and R. Ramesh, in *Interfaces in High- T_c Superconducting Systems*, S. L. Shinde and D. A. Rudman, eds. (Springer-Verlag, New York, 1993), p. 83.
3. H. Xin, D. E. Oates, S. Sridhar, G. Dresselhaus, and M. S. Dresselhaus, *Phys. Rev. B* **61**, 14952 (2000).
4. L. R. Vale, R. H. Ono, and D. A. Rudman, *IEEE Trans. Appl. Supercond.* **7**, 3193 (1996).
5. Y. Habib, C. J. Lehner, D. E. Oates, L. R. Vale, R. H. Ono, G. Dresselhaus, and M. S. Dresselhaus, *Phys. Rev. B* **57**, 13833 (1998).

7. ADVANCED SILICON TECHNOLOGY

7.1 BACK-END-OF-THE-LINE SCALING FOR SILICON-ON-INSULATOR CMOS

For a number of years, we have been involved with a Defense Advanced Research Projects Agency (DARPA) sponsored program to fabricate circuits for industrial, educational, and government contributors. These so-called multiproject circuit runs are fabricated in Lincoln Laboratory's fully planar, 3-level metal, fully depleted silicon-on-insulator (FDSOI) technology. This technology, which fabricates circuits in a thin layer of silicon separated from the wafer bulk by an oxide layer, offers the promise of lower power and faster operation than bulk-fabricated devices.

Multiproject circuit runs have been fabricated in a partially scaled 0.25- μm process, moving now to 0.18 μm . This means that the front end of the process which consists of fabrication up to, but not including, contacts is performed at 0.18- μm design rules. The back end, which goes from contacts to passivation, has been processed with less aggressive 0.5- μm design rules. The major reason for this has been fabrication tool limitations. The consequence of not using a fully scaled process is higher-power, slower circuits due to the increased parasitic RC delay. In June 1999, Hollis Whittington, Group 86, performed a power/speed comparison between Lincoln's 0.25- μm FDSOI process and a fully scaled 0.25- μm process available from the Taiwan Semiconductor Manufacturing Company (TSMC). He found that while Lincoln's FDSOI offered a factor-of-two power savings over the TSMC process, almost another factor of two could be achieved by scaling the back end of Lincoln's process. Acquisition of three critical tools, a state-of-the-art lithography tool, a tungsten deposition tool, and a metal etching tool, has largely removed the impediment to back-end scaling. New back-end design rule goals were established from a combination of the Semiconductor Industry Association (SIA) roadmap and TSMC's 0.25- μm rules. See Table 7-1 for a comparison between current and desired back-end rules.

The scaling of the back end can be broken out into work on a number of process modules: dielectric planarization through chemical mechanical polishing (CMP), contact/via lithography, contact/via etch, dielectric gap fill between conductors, tungsten contact/via plug fill and blanket removal through CMP, and interconnect patterning. Finally, these modules need to be integrated with the front end. This work, which is ongoing, is described below.

For the dielectric planarization module, Lincoln's fully planar process utilizes CMP to planarize dielectric between conductor levels. CMP is a global planarization process and has a length scale of several millimeters. Within-die thickness uniformity is strongly pattern dependent and generally requires a means to ensure uniform pattern density. This is done through the addition of "dummy fill" to conductor layers. These are electrically inactive pieces of conductor added to circuits to meet the density requirement. Ideal values for this density, as reported in the literature, are between 40 and 50%. Lincoln's layouts now incorporate this fill on active, poly, and metal levels. Evaluation of dielectric nonuniformity after metal 1 oxide CMP showed a decrease in thickness variation from 250 to 60 nm from the unfilled design to the filled design.

TABLE 7-1
Design Rules

Process	Current 0.5- μm Process	Scaled 0.25- μm Process
Contact Width	0.5 μm	0.275 μm
Via 1/Via 2 Width	0.60/0.75 μm	0.35/0.35 μm
Contact Aspect Ratio	1	3
Via 1/Via 2 Aspect Ratio	1/0.8	3
Metal 1 Linewidth/Space	0.60/0.60 μm	0.25/0.35 μm
Metal 2 Linewidth/Space	0.60/0.60 μm	0.25/0.35 μm
Metal 3 Linewidth/Space	0.75/0.75 μm	0.25/0.35 μm

In work on the contact/via lithography module, simulations were performed to establish the variables that would give the most focus/dose process latitude in the exposure process. Four courses of action were identified: using an antireflection coating (ARC), using a mask bias and overexposing, thinning the photoresist layer, and reducing the partial coherence of the exposure tool.

Reflectivity from the resist-oxide-substrate stack can cause unwanted contact and via size variation. Of particular concern is the variation of oxide thickness due to the planarization process. A simulation of resist reflectivity vs oxide thickness, with and without an ARC, was performed. Resist thickness was held constant. This plot is shown in Figure 7-1(a). It shows a difference in thickness between a minimum and a maximum in reflectivity in the range of 60 nm. This is certainly within the variation expected from the planarization process. Without an ARC, reflectivity varies from 3 to 25%. Figure 7-1(b) shows a similar plot, but with the addition of an ARC. Reflections in this case have been reduced to between 5 and 15%. The results suggest the need for reflection suppression. The ARC used is an organic-based spin-on layer that has a proven track record in industry. Simulations suggest a thickness of 50 nm.

Experimentally, a number of resists were evaluated for performance. Included was our standard resist Shipley UV5 as well as resist that was specially formulated for contact lithography. In addition, the use of a mask bias was also evaluated. This test used 0.25- μm features that were overexposed to form 0.27- μm contacts. Shown in Figure 7-2 is a plot of exposure latitude vs depth of focus, which clearly shows that our standard resist outperforms the others. It also shows that the mask bias does indeed improve performance. For the 0.27- μm contact drawn at 0.25 μm , and using our standard resist at a thickness of 690 nm, ample process latitude is achieved.

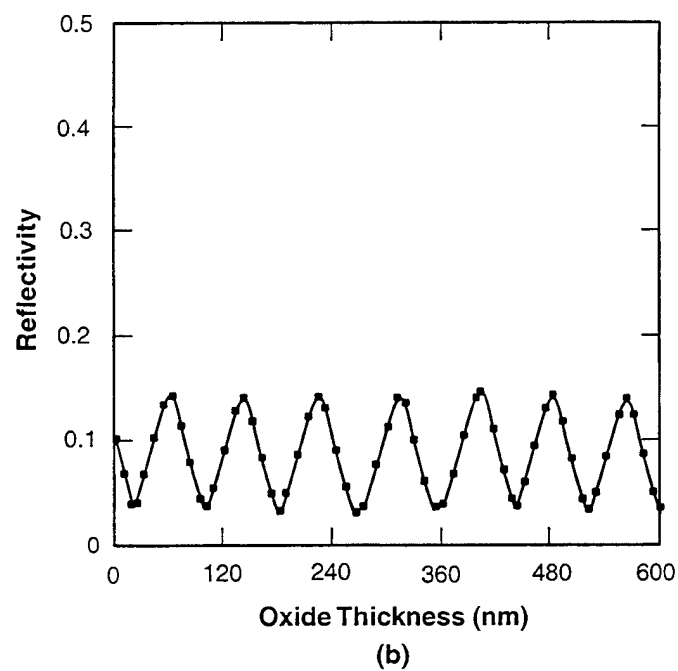
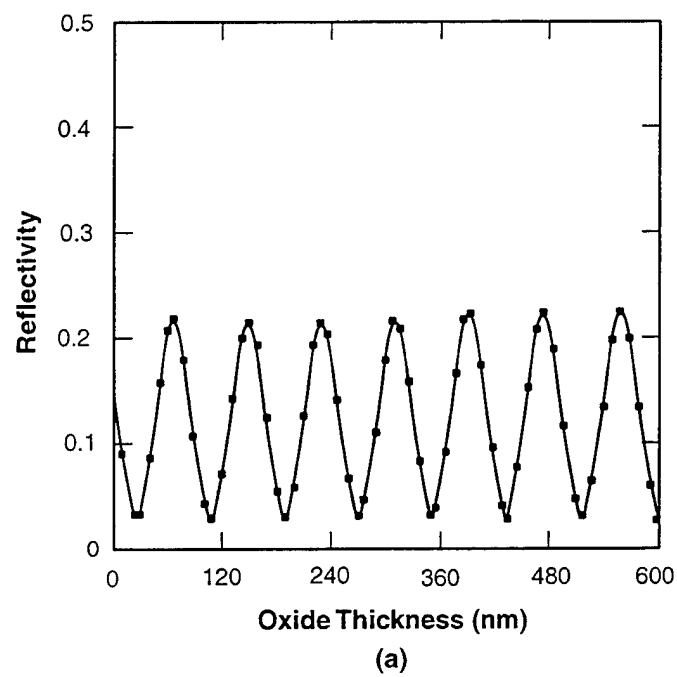


Figure 7-1. Resist reflectivity (a) without antireflection coating (ARC) and (b) with ARC.

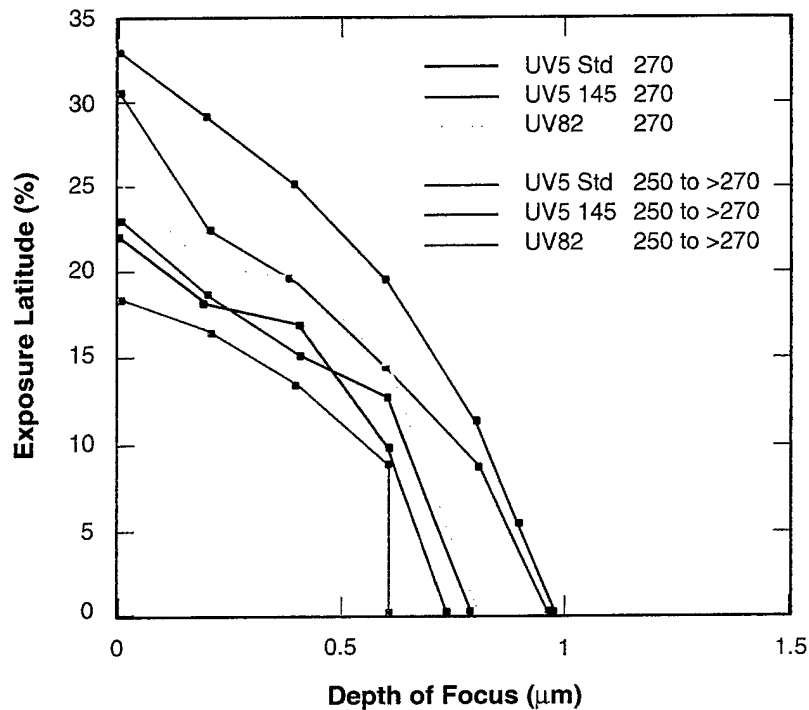


Figure 7-2. Exposure latitude vs depth of focus for different resists and mask biases.

The etch for the contact/via etch module needs to integrate both the ARC and contact or via etch. A contact is a hole etched through the insulating oxide layer to make electrical connections to silicon layers. A via is the same kind of hole to make connections between two metal layers. Since both materials are dry etched in a fluorine-based chemistry, they can be processed in situ. A suitable ARC etch has been developed. Among the goals of a good contact etch are good selectivity to both the resist mask and the underlying stop layer, and uniformity within a few percent. The stop layer consists of silicided silicon for contacts and TiN for vias. The current etch for 0.5- μm contacts uses a CHF_3 , CH_4 , Ar chemistry and has a resist-to-oxide, silicide selectivity of 10 to 1. It was decided that this would be an appropriate etch to scale to 0.275 μm . One well-known effect of dry etching in a relatively high-pressure tool such as is being used is the aspect ratio dependent effect (ARDE). This effect causes contacts with different aspect ratios (depth:width) to etch at different rates. Scaling this etch involved going from 0.5- μm contacts and an oxide thickness of 0.60 μm (aspect ratio: 1.2) to 0.275- μm contacts and a 0.8- μm oxide thickness (aspect ratio: 3). This process was characterized for ARDE by etching three different size contact holes (0.5, 0.35, 0.275 μm) for a sequence of etch times and measuring the amount of material removed. This data was plotted and is shown in Figure 7-3. A strong dependence on aspect ratio is observed. It should be noted that since aspect ratio changes with etch time, the etch rate is not constant. To investigate whether contact size also

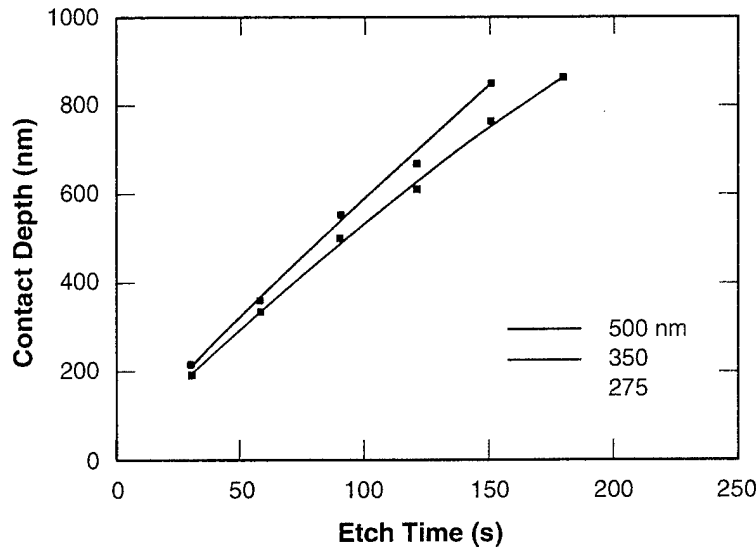


Figure 7-3. Normalized depth vs etch time for contact holes of sizes 500 nm ($y = -0.0065x^2 + 6.503x$), 350 nm ($y = -0.0074x^2 + 6.1097x$), and 275 nm ($y = -0.0094x^2 + 5.8427x$).

influences etch rate, normalized etch rate vs aspect ratio was plotted for the three different size contacts. This is shown in Figure 7-4. The plot clearly shows that the etch rate is a function of aspect ratio only. Figure 7-5 shows a scanning electron micrograph (SEM) cross section of a 0.27- μm contact etched in 0.8 μm of oxide.

In work on the dielectric gap fill module, plasma-deposited oxide is used as the dielectric between levels of metal. It is important that this film be deposited uniformly between conductors, leaving no voids. Voids can be exposed during the planarization process and subsequently trap contaminants. Scaling the back end means smaller gaps and hence higher aspect ratios. In the proposed process the aspect ratio will increase from 1.05 to 1.8. Depositing a void-free dielectric in a plasma process is inherently problematic owing to the low surface mobility of the depositing oxide film. Voids between conductors form as the film pinches off. One way to deal with this situation is to use a combination of deposition and etchback cycles in film deposition in the Electrotech Delta system. The etchback cycle, which consists of an argon sputter, preferentially etches the overhanging top corners of the oxide and allows better line of sight for the depositing species on the next cycle. Film thickness and etchback time for a given cycle depend on the number of cycles used. The unscaled process utilized four cycles of deposition/etchback and was able to fill an aspect ratio of 1.05. For the fully scaled back end the number has been increased to ten. This allows filling up to an aspect ratio of ~1.7–1.8, which is the target value.

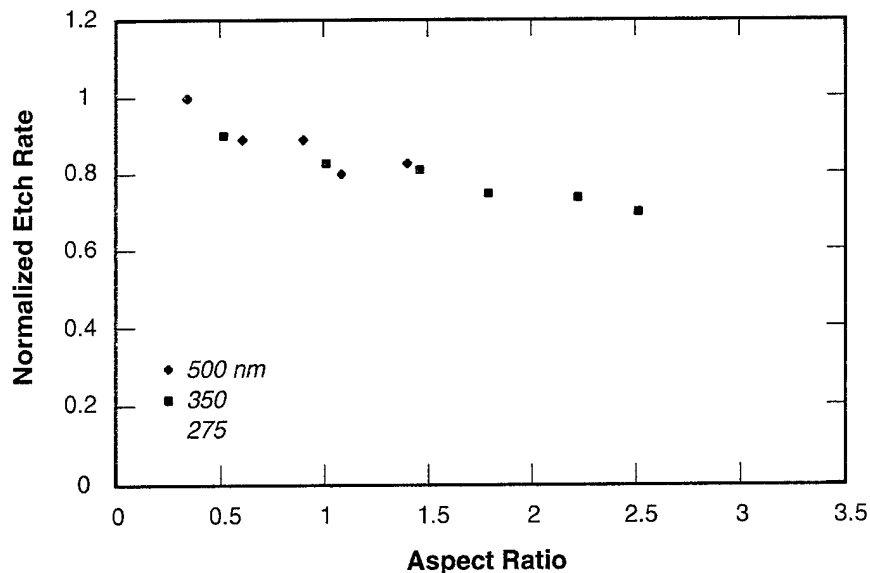


Figure 7-4. Normalized etch rate vs aspect ratio for contact holes of sizes 500, 300, and 200 nm.

An important part of a multilevel conductor process, used for the tungsten contact/via plug fill and CMP module, is ensuring that different levels are electrically connected. These are done through contact and via holes. It is desired that the holes be nearly vertical for increased packing density. This constraint as well as the growing aspect ratio makes it very difficult to fill these holes with metal through the typical sputtering deposition method. Like the plasma oxide process, the sputtering process has poor step coverage, typically only ~20% for an aspect ratio of 0.5. The fully scaled process needs to fill holes with an aspect ratio of 3. The industry-proven method of dealing with this problem is to separate the contact/via plug from the interconnect deposition. The plug metal consists of thermally activated tungsten chemical vapor deposition. This process is extremely conformal, and allows 100% filling in aspect ratio holes of >5:1. Lincoln recently acquired and installed a tungsten deposition tool (Applied Materials P-5000), and the plan is to transfer the existing Al plug process to a tungsten plug. The existing Al process has performed marginally and is not suitable for the higher aspect ratio of a fully scaled process.

Crucial to the tungsten process is a TiN/Ti barrier/glue layer deposited by sputtering (that is, a layer of Ti is deposited followed by a layer of reactively sputtered TiN). This layer must be continuous in the contact/via. The layer is the real limiting factor to the tungsten plug, as it suffers from the step coverage issues inherent in sputtering. An advantage of our sputtering tool (Trikon Sigma) is that the metal flux is collimated, which improves step coverage. It has been estimated that this tool should be able to scale to 0.20- μ m contacts with an aspect ratio of 4:1.

stack is performed in a state-of-the-art, low-pressure, high-ion-density Trikon tool in a BCl_3 , Cl_2 , N_2 chemistry. In developing an etch, one can vary a number of parameters, including source power, wafer bias power, gas flows and ratios, and etch pressure. Important aspects of a good etch are producing straight smooth sidewalls, good selectivity to the resist mask and underlying oxide stop layer, no conducting etch residue, and good electrical isolation from adjacent metal runs. Statistical tests, performed by the tool vendor, have shown general trends in how these results are affected by the etch variables.

Metal etching in this tool is very pattern dependent, requiring new etch development for each pattern. It is much easier to fix the pattern density through the addition of dummy fill and develop only one etch. In fact, the need is complementary with the need for dummy fill in dielectric CMP for uniformity issues. It turns out that the fill serves both purposes, and an etch has been developed for ~40–50% pattern density.

The new etch meets and actually exceeds the needs of the scaled process. It has a metal/resist selectivity of 1.6, an oxide loss of ~25 nm, and a linewidth variation of <1%, 1σ , both dense and isolated, across a 150-mm wafer. A line/space pair of 0.17/0.225 μm with an aspect ratio of ~3 has been successfully etched. Measurements of snake and comb test devices verified line continuity and electrical isolation. Figure 7-7 shows SEM micrographs of this structure.

In summary, Lincoln's 3-level metal, fully planar, partially scaled FDSOI process offers lower power and faster operation than bulk CMOS. However, a further factor-of-two savings in power can be achieved by scaling the back end. This entails developing and/or modifying process modules such as contact/via lithography and etch, interconnect gap fill, tungsten plug fill, and interconnect processing. Recent tool acquisitions have removed impediments to this endeavor. Most modules have now achieved proof of concept. The next step is integrating the new back end with the existing process and fine tuning.

J. M. Knecht	D. K. Astolfi
R. J. Bicchieri	C. K. Chen
M. Fritze	P. M. Gouker
C. L. Keast	K. L. Newcomb
V. Suntharalingam	L. Travis
P. W. Wyatt	D.-R. Yost

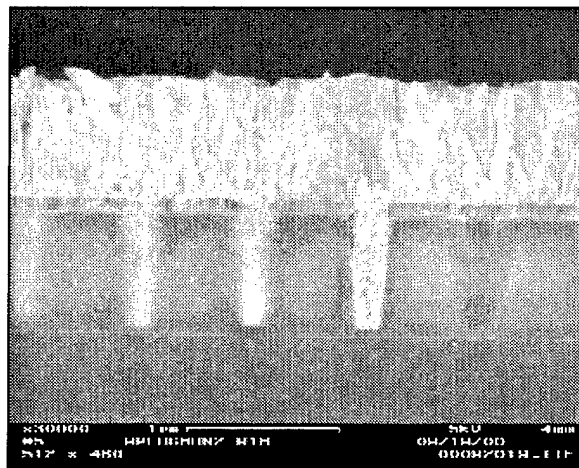


Figure 7-6. Cross-sectional SEM of 0.27- μm tungsten-filled contact plug.

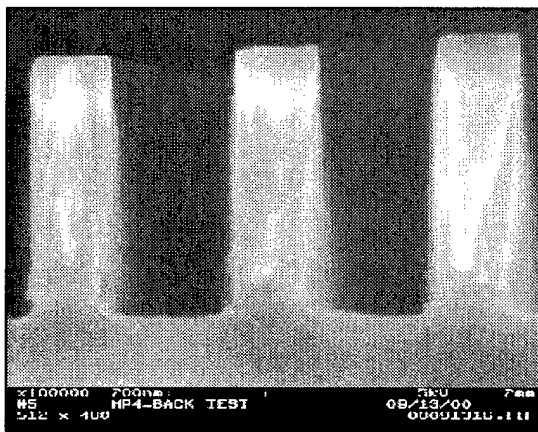
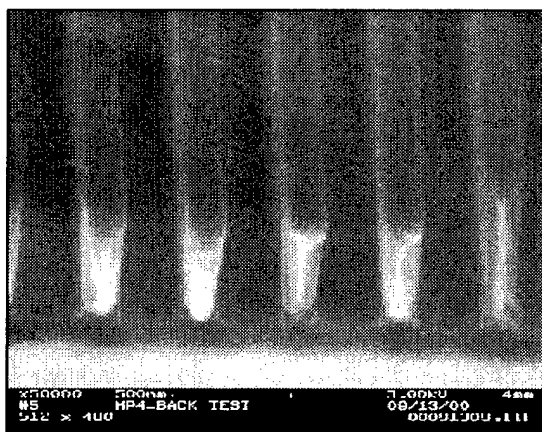


Figure 7-7. SEMs of 0.17/0.225- μm etched metal stack.

